J. Fluid Mech. (1995), *vol.* 300, *pp.* 169–205

Bifurcation of swirl in liquid cones

By VLADIMIR SHTERN AND ANTONIO BARRERO
Department of Energy Engineering and Fluid Mechanics, University of Seville,
E-41012 Seville, Spain

(Received 15 March 1994 and in revised form 4 May 1995)

We show that rotation appears owing to bifurcation in primarily pure meridional steady motion of viscous incompressible fluid. This manifestation of the laminar axisymmetric 'swirl dynamo' occurs in flows inside liquid conical menisci with the cone half-angle $\theta_c < 90°$. The liquid flows towards the cone apex near the surface and moves away along the axis driven by (i) surface shear stresses (typical for electrosprays) or (ii) by body Lorentz forces (e.g. in the process of cathode eruption). When the motion intensity increases and passes a critical value, new swirling regimes appear resulting from the supercritical pitchfork bifurcation. This agrees with recent observations of swirl in Taylor cones. We find that when the swirl Reynolds number Γ_c reaches a threshold value, flow separation occurs and the meridional motion becomes two-cellular with inflows near both the surface and the axis, and an outflow near the cone $\theta = \theta_s$, $0 < \theta_s < \theta_c$. In the limit of high Γ_c, the angular thickness of the near-surface cell tends to zero. In case (i) the swirl is concentrated near the surface while the motion inside the inner cell becomes purely meridional with the radial velocity being uniform. We also study the two-phase flow of a liquid inside and a gas outside the meniscus. Flow separation occurs in both media and then swirl is concentrated near the interface. In case (ii) we reveal another interesting effect: a cascade of flow separations near the axis. As the driving forces increase, meridional motion becomes multi-cellular although very slow in comparison with swirl. To cover all ranges of parameters we combine numerical calculations and asymptotic analyses.

1. Introduction

1.1. *Review of previous studies of swirl generation*

The appearance of swirl due to bifurcation of a primarily non-swirling flow ('*swirl dynamo*') seems to be a more striking and intriguing manifestation of symmetry breaking in comparison with, for example, heat convection onset and even the hydromagnetic dynamo. The reason is the conservation law of angular momentum. For the swirl dynamo to occur, a separation mechanism or a source of angular momentum must start to act at critical values of control parameters.

The problem of swirl generation has been widely discussed for the case of the bathtub vortex, see e.g. Ogawa (1993). It is still questionable whether this phenomenon relates to symmetry breaking or external forcing; however, there are experimental results in favour of the former. A steady flow toward a sinkhole at the bottom centre of a rectangular box was experimentally studied by Kawakubo *et al.* (1978). When the flow rate exceeds a threshold value, rotation is observed and its intensity depends on the flow rate as at a supercritical bifurcation. Torrance (1979) observed swirl generation in a confined flow. In this experiment, thermal convection is induced in a sealed can by a local source of heat at the centre of the bottom. Also, there is a temperature gradient at the sidewall, corresponding to stable stratification. There is a pure meridional circulation with an ascending jet near the axis and descending flow along the sidewall; however, at some parameter values, the jet begins to rotate. An interesting phenomenon occurs in a glass of water that oscillates in a horizontal direction: at some values of the oscillation amplitude and frequency, the surface wave begins to rotate (see a review and recent experiments in Funakoshi & Inoue 1988).

Observations have been made of swirl generation in flows of conducting liquids driven by surface (Fernandez de la Mora, Fernandez-Feria & Barrero 1991; Fernandez-Feria, Fernandez de la Mora & Barrero 1995; and A. Gomez 1992, personal communication) or body (Bojarevics *et al.* 1989) electrical forces; these experiments are closer to this paper's subject. Surface-stress-driven flows (SSF) are related to so-called Zeleny–Taylor cones. Zeleny (1917) found that the meniscus of a conducting liquid at the exit of a capillary tube takes a conical shape when the tube is charged to a sufficiently high potential. Taylor (1964) explained that this shape is the result of a balance between the action of electrical pressure and surface tension when the liquid is at rest. In a small vicinity of the cone apex, destruction of the liquid surface takes place and a thin jet or spray erupts; the jet diameter may be more than 10^3 times smaller than the inner diameter of the capillary tube (Fernandez de la Mora 1992). In recent years, this phenomenon has attracted the attention of many researchers because of a wide and rapidly growing area of electrospray applications – from paint spraying and jet printing to fuel atomization and biotechnology (Bailey 1988; Fenn *et al.* 1989). As a result, striking new features have been revealed. In contrast to earlier conjectures that the flow inside the cone is always unidirectional, experiments discovered a circulatory meridional motion (Hayati, Bailey & Tadros 1986*a*, *b*). This circulation is driven by surface shear stresses $\tau_{\theta r} = \epsilon_0 E_\theta E_r$. Here ϵ_0, E_θ and E_r are the vacuum permittivity, and the normal and tangential components of the electric field at the liquid surface, respectively. For liquids with a high electrical conductivity, $\tau_{\theta r}$ is so small that no noticeable circulatory motion appears and the liquid inside the cone moves as a purely radial sink (Fernandez de la Mora & Loscertales 1994). However, for liquids with a small electrical conductivity and viscosity, $\tau_{\theta r}$ induces the circulatory motion. The liquid moves towards the apex along the meniscus surface but away from the apex near the axis. In addition to this meridional flow we have observed swirl inside Taylor cones. Fernandez-Feria *et al.* (1995) have considered, in the boundary layer approximation, the liquid motion driven by surface shear stresses $\tau_{\theta r} \sim r^n$, where r is the distance from the apex. Gañan-Calvo (1995) has proposed $n = -5/2$ (see also Barrero *et al.* 1995*a*) since $E_r \sim r^{-2}$, owing to electrical conduction through the bulk, and $E_\theta \sim r^{-1/2}$ (Taylor 1964). Barrero *et al.* have shown that the assumption of high Reynolds numbers is well satisfied for motions inside Taylor cones of liquids with sufficiently small conductivity and viscosity.

A different mechanism which may be speculatively thought of as the driving force for the circulation inside Taylor cones is the electric Marangoni effect (EME). The Marangoni effect is the appearance of shear stresses due to a gradient of surface tension. Similar to temperature and surfactant concentration, an electric field changes the density of free energy at the liquid surface and therefore changes the surface tension. EME yields the surface stress distribution with $n = -2$ (Shtern & Barrero 1994).

We assume here that $\tau_{\theta r} \sim r^{-2}$, which allows us to describe the induced flow by applying the conical similarity class of exact solutions of the Navier–Stokes equations (NSE), i.e. to reduce the NSE to a system of ordinary differential equations (ODE). It is worth noting that, independently of the physical nature of the driving forces and the

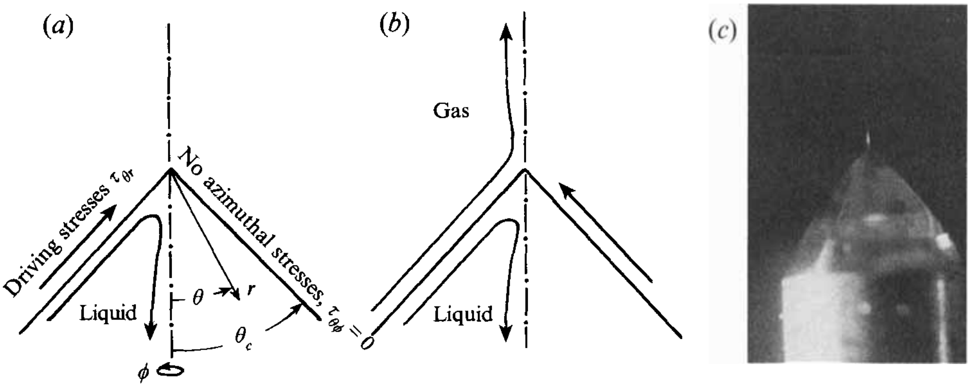

FIGURE 1. Schematics of (*a*) one-medium and (*b*) two-medium problems when the motion is driven by surface shear stresses $\tau_{\theta r}$ and (*c*) photograph of a conical meniscus. Azimuthal stresses at the surface $\tau_{\theta\phi}$ are zero in the one-medium case and continuous in the two-medium case. The coordinates, typical streamlines and shear stress directions are shown.

exact value of exponent n, the conically similar solutions of the NSE, which provide a description of the motion at finite Reynolds numbers as well, are not just interesting themselves but can also serve as a reference for the more general case of arbitrary n which needs the full NSE and can be reduced to ODE only in the boundary layer approximation. Figure 1 shows the schematics of (*a*) the one- and (*b*) two-medium problems considered here together with (*c*) a photograph of a conical meniscus. For completeness the whole range $(0, \pi)$ of the liquid cone half-angle θ_c is considered; however, we find that the laminar axisymmetric swirl dynamo occurs only for $\theta_c < \pi/2$. Some preliminary results for the one-medium SSF have been reported in Shtern, Goldshtik & Hussain (1994). Here these results are substantially extended by flow separation and asymptotic analyses, and also the quite new two-medium problem is studied.

For very high (metallic) conductivity, the meridional motion is driven by electromagnetic (Lorentz) body forces. Conical menisci of a high-conducting medium arise on the cathode surface of plasmatrons and in electric arcs (Bojarevics *et al.* 1989). It is not easy to study the flow inside the menisci under controlled conditions; nevertheless, there are some intriguing experimental results. One such experiment (using a planar free surface) is described in Bojarevics *et al.* (1989). Mercury filling a hemispherical copper container (36 cm in diameter) is in meridional motion converging to the axis near the free surface, being directed down near the axis and up along the wall. This circulation is driven by the electric current from a small electrode situated in the centre of the free surface, with the wall serving as the second electrode (see the schematic in figure 2*a*). If the electric current $J < 15$ A, then no swirl is observed; but for $J > 15$ A, the meridional motion is accompanied by swirl which increases with J. There is no obvious external force which can produce the observed rotation. The Earth's magnetic field seems not to be the cause since the flow diverging near the free surface does not rotate even at the maximum current in the experiment, $J = 1500$ A. The strongest argument in favour of swirl generation due to symmetry breaking is that there is the threshold value of J for the onset of rotation. Here we consider a generalized and idealized problem for body-force-driven flows (BFF): the free surface is considered to be conical with the cone half-angle in the range $0 < \theta_c \leqslant \pi/2$, and the conical region is supposed to be infinite (figure 2*b*). We study (i) how to control flow patterns in the menisci with the help of rotation driven by a given circulation at the free surface and

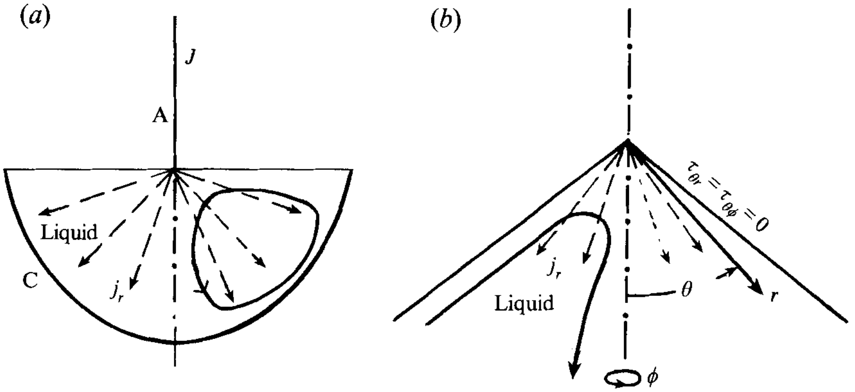

FIGURE 2. Schematics of (*a*) experiment by Bojarevics *et al.* (1989) and (*b*) theoretical problem when the motion is driven by body forces. The dashed rays with arrows show a spherically uniform electric current and the curves with arrows show typical streamlines. In the experiment, the liquid (mercury) also rotates when the electric current J from electrode A (rod) to electrode (C) (copper wall) exceeds 15 A.

(ii) the possibility of a swirl dynamo when the surface is shear stress free, and rotation appears as a result of bifurcation.

Previous theoretical predictions of self-rotation were related to unsteady motions (Funakoshi & Inoue 1988; Goldshtik, Shtern & Zhdanova 1984) or some turbulence models (Goldshtik & Shtern 1988, 1990). Here we show that swirl generation can also be predicted in laminar flow by bifurcation analysis of steady axisymmetric solutions of the NSE for both the SSF and BFF cases. Looking for bifurcation of the SSF we consider the primary non-swirling flows corresponding to analytical solutions found by Yatseev (1950) and Squire (1952). Features of new self-swirling flows are compared with that of the forced-swirling flows studied by Goldshtik & Shtern (1990).

The primary non-swirling flows in the BFF case correspond to the self-similar solutions of the NSE with meridional body forces. These flows were predicted by Zhigulev (1960) and studied by Lundquist (1969), Shcherbinin (1969), Shercliff (1970), Sozou (1971), Narain & Uberoi (1971) and others. (We refer the reader to more detailed reviews by Bojarevics *et al.* 1989 and Petrunin & Shtern 1993.) Two intriguing effects were found: (i) collapse and (ii) inversion of the meridional flow by an imposed rotation. The collapse means a loss of the existence of similarity solutions due to the appearance of a singularity at the axis. For one-cell MHD flow without rotation, the collapse was first found by Sozou (1971) for a half-space region and by Narain & Uberoi (1971) for cones. The inversion, which is a kind of internal flow separation, was found by Bojarevics, Sharamkin & Shcherbinin (1977) in the problem when rotation was forced by a particular distribution of the axial magnetic field. Since both effects are found to be rather closely related to the swirl dynamo problem, we study, in addition to the self-swirling regimes, forced-swirling flows with given circulation at the cone surface to examine the following new effects: a cascade of internal flow separations and a collapse of multi-cell regimes.

1.2. *Observation of swirl in Zeleny–Taylor cones*

As we mentioned above there have been observations of swirl in Zeleny–Taylor cones. Before the following theoretical study we report here our recent observations of this phenomenon. Photographs in figure 3 show trajectories of air bubbles inside an electrified meniscus. The flow is a combination of a meridional motion and swirl

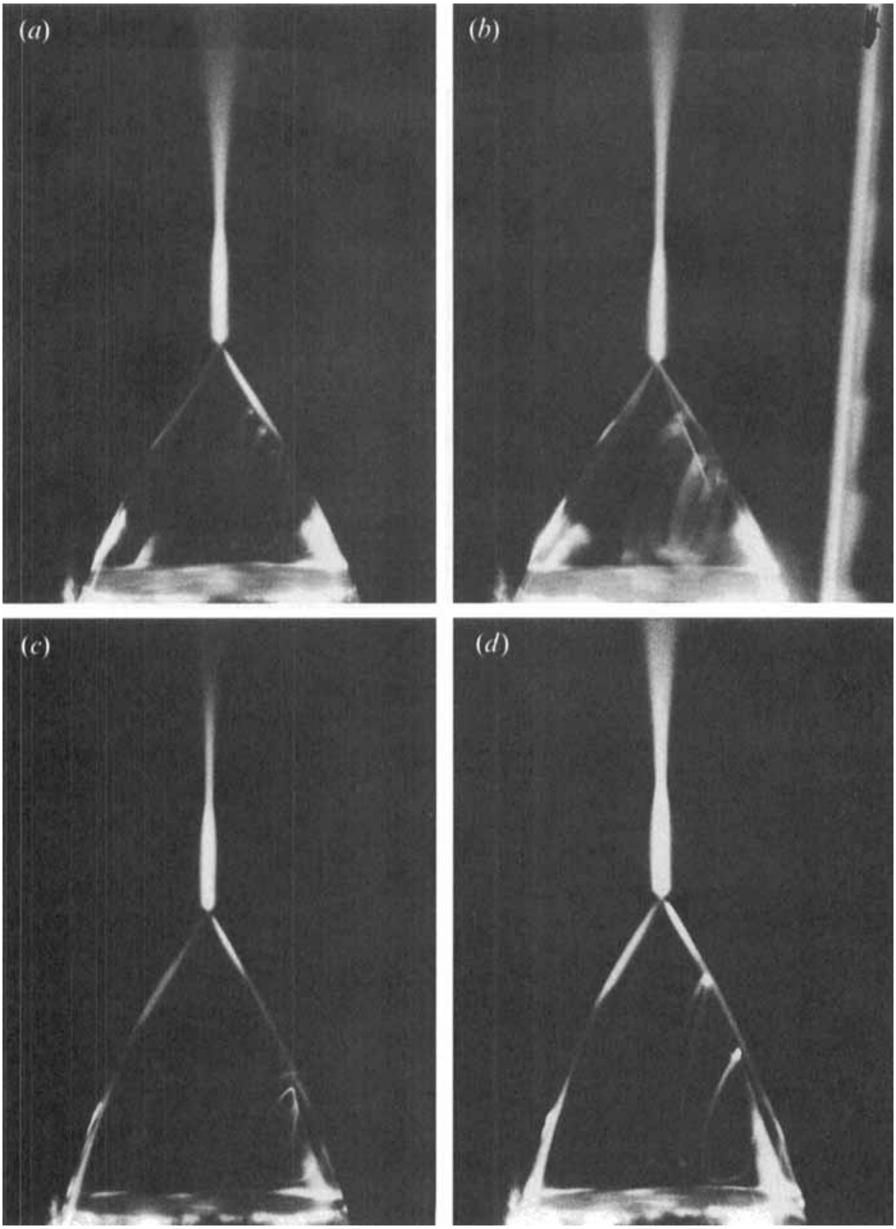

FIGURE 3. Air bubble paths inside electrified heptane menisci. The ejected flow rate, $Q = 3.9 \times 10^{-10}$ m^3 s^{-1} was the same for the four cases (*a–d*). Two values of electrical potential difference between needle and ground electrode were applied: the one corresponding to (*a*) and (*b*) being smaller than that for (*c*) and (*d*).

although there is no obvious swirl forcing. The liquid (heptane doped with a small amount of the antistatic Stadis 450, Du Pont, for enhancing of its electric conductivity) is injected through a capillary needle (0.35 mm inner radius) connected to a potential of 4 KV relative to the ground electrode. Outside the needle, a nearly conical meniscus forms and a jet is emitted from its vertex. The parameters are: the liquid density of 684 kg m^{-3}, viscosity of 4.6×10^{-4} kg m^{-1} s^{-1}, surface tension of 21×10^{-3} N m^{-1}, electrical conductivity of 2×10^{-6} S m^{-1}, and flow rate 3.9×10^{-10} m^3 s^{-1}. The estimated

Reynolds number is of order 100 (Fernandez-Feria *et al.* 1995). For such values our theory predicts one more effect, which has not been yet observed in experiment: flow separation.

2. General problem formulation

2.1. *Reduction to a boundary value ODE problem*

We consider steady flows of a viscous incompressible fluid possessing conical similarity and admitting the representation

$$v_r = -\frac{\nu\psi'(x)}{r}; \quad v_\theta = -\frac{\nu\psi(x)}{r\sin\theta}, \quad v_\phi = \frac{\nu\Gamma(x)}{r\sin\theta},$$

$$\Psi = \nu r\psi(x), \quad p = p_\infty + \frac{\rho\nu^2 q(x)}{r^2}, \quad \boldsymbol{F} = \frac{\rho\nu^2 \boldsymbol{f}(x)}{r^3}, \quad x = \cos\theta. \tag{1}$$

Here (r,θ,ϕ) are the spherical coordinates; r is the distance from the origin; θ and ϕ are polar and azimuthal angles (see figures 1 and 2); v_r, v_θ, v_ϕ, Ψ, p, ρ, ν and $\boldsymbol{F}$ are velocity components, Stokes stream function, pressure, density, kinematic viscosity and external body force, respectively; ψ, Γ, q and $\boldsymbol{f}$ are dimensionless functions; the prime denotes differentiation with respect to x. Studying the possibility of spontaneous generation of swirl, we assume that the azimuthal component of the body force is zero, $f_\phi = 0$, i.e. there is no external forcing of the azimuthal motion.

Substitution of (1) into the Navier–Stokes equations, exclusion of pressure and simple calculations yield

$$(1-x^2)\psi^{\mathrm{iv}} - 4x\psi y''' - (\psi^2/2)''' = 2\Gamma\Gamma'/(1-x^2) - 2f_\theta(1-x^2)^{-1/2} + f_r', \tag{2}$$

$$(1-x^2)\Gamma'' = \psi\Gamma'. \tag{3}$$

The boundary conditions at the axis, $x = 1$, follow from representation (1) and the requirement of velocity boundedness:

$$\psi(1) = 0, \tag{4}$$

$$|\psi'(1)| < \infty, \tag{5}$$

$$\Gamma(1) = 0. \tag{6}$$

Note that condition (5) is not trivial because $x = 1$ is a singularity point for equation (2). Three other conditions have to be satisfied at the cone surface, $x = x_c$. They need to be discussed in more detail.

2.2. *Conditions at the cone surface*

The first of these conditions is the impermeability requirement,

$$\psi(x_c) = 0. \tag{7}$$

The other two conditions concern the shear stresses,

$$\tau_{\theta r} = [(1-x^2)\psi'' + 2\psi]\rho\nu^2(r^2\sin\theta)^{-1}, \tag{8}$$

$$\tau_{\theta\phi} = [(1-x^2)\Gamma' + 2x\Gamma]\rho\nu^2(r^2\sin^2\theta)^{-1}. \tag{9}$$

A value of the radial stress, $\tau_{\theta r}$, is given at the surface, and taking into account (7) and (8) this condition can be written in the form

$$(1-x_c^2)^{1/2}\psi''(x_c) = -Re_\tau, \tag{10}$$

where dimensionless parameter $Re_\tau = -r^2\tau_{\theta r}/(\rho\nu^2)$ characterizes the intensity of the surface forcing and is a kind of Reynolds number. The 'minus' sign is used to make Re_τ positive when $\tau_{\theta r}$ is directed towards the origin (this direction is relevant for this paper's context). When the motion is driven by body forces we assume that the surface is free, i.e. $Re_\tau = 0$.

The requirement that there is no forcing of the azimuthal motion at the cone surface and (9) give

$$(1-x_c^2)\,\Gamma'(x_c)+2x_c\,\Gamma(x_c) = 0. \tag{11}$$

(This is valid for the one-medium problem; in the two-medium case, $\tau_{\theta\phi}$ must be just continuous across the interface, see §3.)

Note that the normal stresses induced by the motion are not zero at the liquid surface. They are balanced by surface tension which makes the meniscus shape not exactly conical. This distortion is neglected here for the reasons discussed below.

The form of the liquid surface is the result of the normal stress balance, $\sigma_e+\sigma_\gamma+\sigma_m = 0$. Here the terms are contributions from the electric field, surface tension, and motion, respectively. Without motion, the balance gives the conical form of the liquid meniscus (Taylor 1964). To estimate the role of σ_m one has to take into account that the motion is driven by $\tau_{\theta r}$. Therefore σ_m and $\tau_{\theta r}$ are of the same order of magnitude. The shear stresses are induced by the electric field, and ratio $\tau_{\theta r}/\sigma_e$ is proportional to E_r/E_θ. Here E_r and E_θ are the tangential and normal components of the electric field at the liquid surface, respectively. For menisci of electrosprays, the liquid surface is nearly equipotential, which means that the electric field is nearly normal to the surface, i.e. $E_r/E_\theta \ll 1$.

The value of E_r depends on the electric conductivity K: $E_r \sim I/(Kr^2)$. Taylor found that $E_\theta \sim \gamma^{1/2}(\epsilon_0 r)^{-1/2}$, where γ is the liquid–gas surface tension. For polar liquids, Fernandez de la Mora & Loscertales (1994) experimentally found that $I \sim f(\beta)(QK\gamma)^{1/2}$, where Q is the flow rate and f is an empirical function of the liquid to vacuum permittivity ratio β. Gañan-Calvo (1995) has theoretically found $f(\beta) \sim \beta^{-1/4}$ which has been experimentally corroborated by Barrero, Gañan-Calvo & Davila (1995*b*). Therefore $E_r/E_\theta \sim (Q\epsilon_0)^{1/2}(r^3K\beta^{1/2})^{-1/2}$. Typical values for the electrospraying of methanol are: $Q = 10^{-10}\ \mathrm{m^3\,s^{-1}}$, $K = 8.5\times10^{-5}\ \mathrm{S\,m^{-1}}$, $\beta = 33.6$, and a typical needle radius is 5×10^{-4} m. This yields $E_r/E_\theta \sim 10^{-4}$. For non-polar liquids, we can use directly experimental values of I (Barrero *et al.* 1995*a*) obtained for electrospraying a mixture of heptane dopped with a small amount of the antistatic Stadis 450, with $K = 2\times10^{-6}\ \mathrm{S\,m^{-1}}$, $\gamma = 0.021\ \mathrm{N\,m^{-1}}$. For $Q = 10^{-9}\ \mathrm{m^3\,s^{-1}}$, and voltage 4200 V, the measured current was $I = 18\times10^{-9}$ A. Then $E_r/E_\theta \sim 0.016$ near the needle and $E_r/E_\theta < 0.2$ for $r > 0.9\times10^{-4}$ m.

Thus, in typical electrosprays $\sigma_m/\sigma_e \ll 1$ and, therefore, the motion influence on the meniscus shape is very small. This supports our approximation where σ_m is neglected in the above balance and the liquid surface is conical and fixed. Photographs of the electrospray menisci (e.g. see Shtern & Barrero 1994 and the photographs in this paper) show that the liquid surface is indeed nearly conical.

In the case of body forces, the surface shape is governed by the same terms and the motion contribution can be again negligible. Bojarevics *et al.* (1989) did not observe any significant distortion of the liquid metal surface induced by the motion. This supports our idealization that the liquid surface is not disturbed by the motion in the body-force problem.

2.3. *Introduction of an auxiliary function*

Thus, conditions (4)–(7), (10), and (11) close the boundary value problem for system (2) and (3). To simplify our analysis, it is useful (following Goldshtik 1960) to introduce an auxiliary function F, denoting the right-hand side of (2) as F''', so that

$$(1-x^2)F''' = 2\Gamma\Gamma' - 2f_\theta(1-x^2)^{1/2} + (1-x^2)f'_r. \tag{12}$$

This allows integration of (2) three times yielding

$$(1-x^2)\psi' + 2x\psi - \psi^2/2 = F. \tag{13}$$

As we will apply (12) and (13) instead of (2), it is useful to formulate boundary conditions for F. Two of the boundary conditions are at the axis,

$$F(1) = F'(1) = 0, \tag{14}$$

which follow from (4), (5), (13), and the first derivative of (13),

$$(1-x^2)\psi'' + 2\psi - \psi\psi' = F'. \tag{15}$$

The third condition is at the surface. Evaluating (15) at $x = x_c$ and taking into account (7) and (10), we have

$$F'(x_c) = -Re_\tau(1-x_c^2)^{1/2}. \tag{16}$$

Therefore, when the body forces and circulation are given, one can find F by integrating (12) with conditions (14) and (16). We will use this in our asymptotic analyses.

2.4. *Possibility of swirl bifurcation*

Equation (3) with conditions (6) and (11) has the trivial solution $\Gamma \equiv 0$. Our goal is to find a non-trivial solution and to study when such a solution branches from the trivial one. The necessary condition for such a bifurcation is that problem (3), (6) and (11) has a non-zero solution at a given ψ. This corresponds to an infinitesimal value of the swirl Γ when the influence of Γ on ψ is negligible. Since the existence of the non-zero solution depends on ψ, its nature itself needs to be analysed first.

In this linear (with respect to swirl) problem, the term $2\Gamma\Gamma'$ in (12) is neglected, and integration of (12) with conditions (14) and (16) gives F independent of ψ. To find ψ one needs to integrate (13) with condition (7). (Conditions (4) and (5) are satisfied automatically due to (14).) Equation (13) can be transformed into a linear one by introducing a new variable U, such that

$$\psi = -2(1-x^2)\,U'/U. \tag{17}$$

Substitution of (17) in (13) yields

$$U'' + \tfrac{1}{2}F(1-x^2)^{-2}\,U = 0, \tag{18}$$

and we apply the conditions

$$U(x_c) = 1, \quad U'(x_c) = 0. \tag{19}$$

The first condition (normalization) is formulated without any loss of generality, since, according to (17), $U(x)$ is determined up to an arbitrary numerical factor. The second condition (19) follows from (7) and (17). Thus, we have to solve the initial-value problem (18) and (19) in the interval $x_c \leqslant x \leqslant 1$. For ψ to be bounded, U must not become zero inside the interval.

At zero forcing, $F \equiv 0$, the solution is $U \equiv 1$, and therefore for small F there is no zero of U inside the interval. For the swirl-free SSF flows, F is found explicitly as follows from (12), (14) and (16):

$$F = \tfrac{1}{2}F''(1)(1-x)^2, \quad F''(1) = Re_\tau[(1+x_c)/(1-x_c)]^{1/2}.$$

For $Re_\tau > 0$, we see that $F \geqslant 0$. Also for the non-swirling BFF flows, it will be shown in §4.6.1 that $F \geqslant 0$. When F is positive, curvature U'' is negative for $U > 0$ owing to (18). Then it follows from (19) that U' is negative for $x > x_c$ and $|U'|$ increases with x. Therefore, $U(x)$ must pass zero at some $x = x_p$. Because of (17), this means that ψ has a pole at $x = x_p$. While F is small, the pole is outside the interval, i.e. $x_p > 1$. As F increases, x_p approaches and can pass the interval boundary $x = 1$. The event when x_p reaches 1 is called *collapse*. In a near-collapse situation, a strong jet forms flowing away from the origin near the axis, and the axial velocity becomes infinite at the collapse. It has been shown that collapse does occur in the cases of both surface (Goldshtik & Shtern 1990) and body (Sozou 1971; Narain & Uberoi 1971) forcing. We will show now that the collapse phenomenon is closely related to the swirl dynamo.

Substituting (17) in (3) and integrating we get $\Gamma' = \Gamma'(x_c)\,U^{-2}$. Then integrating once more, using the normalization $\Gamma(x_c) = 1$ (which is possible in this linear problem), and condition (11) we find that

$$\Gamma(1) \equiv \Gamma_1 = 1 - 2x_c(1-x_c^2)^{-2}\int_{x_c}^{1} U^{-2}\,\mathrm{d}x. \tag{20}$$

Since we have to satisfy (6), (20) gives a necessary condition for a swirl dynamo: $\Gamma_1 = 0$. It is evident from (20) that the swirl dynamo is impossible when $x_c \leqslant 0$ because $\Gamma_1 > 0$. However, when $x_c > 0$, Γ_1 can change its sign as the forcing intensity increases. At $F \equiv 0$ ($U \equiv 1$) it follows from (20) that $\Gamma_1 = (1-x_c)/(1+x_c) > 0$ because $|x_c| < 1$. Therefore, there is no swirl dynamo for a weak forcing. On the other hand, on approaching the collapse, the integral in (20) tends to infinity and Γ_1 is negative. As Γ_1 is a continuous function of the forcing intensity, there must be a specific value of the intensity at which the swirling regimes bifurcate. We show below that this bifurcation does occur for both the SSF and BFF cases.

3. Surface forcing

3.1. *Reformulation of the problem for the two-medium case*

Now we formulate the problem to consider both a liquid flow inside the meniscus, $x_c \leqslant x \leqslant 1$, and a gas flow outside the meniscus, $-1 \leqslant x \leqslant x_c$. Also, we consider the one-medium case when the influence of the gas flow on the liquid motion is neglected. The one-medium problem is a particular case of the two-medium one in the limit $\rho_g/\rho_l \rightarrow 0$ where subscripts g and l denote gas and liquid. We consider the interface fixed at $x = x_c$ and supported by surface tension in accordance with Taylor's theory. Deformation of this surface due to the normal stresses induced by the motion is neglected. At $x = x_c$, the shear stress $\tau_{\theta r}$ is different for liquid and gas at the surface because the external tangential forcing is applied to the liquid surface in the radial direction. However, $\tau_{\theta\phi}$ must be continuous across the surface and so must v_r, v_ϕ, and v_θ (the latter is zero at $x = x_c$ from both sides). In such a formulation, a swirl-free flow inside the meniscus is totally independent of an ambient gas flow, but the gas flow is induced by the liquid one owing to the continuity of v_r. The gas flow is also influenced by the emitted jet and drops, and taking this into account greatly complicates the problem. However, electrosprays are rather dilute in many cases so, considering our approach as a first step in simplifying the real situation, we neglect this effect here.

To analyse the problem, it is convenient to apply representation (1) using liquid viscosity ν_l and density ρ_l in the meniscus, and gas viscosity ν_g and density ρ_g outside. Then the continuity requirements for $\tau_{\theta\phi}$ and the velocity components take the form

$$\left.\begin{array}{l} (1-x_c^2)\,\Gamma'_g(x_c)+2x_c\,\Gamma_g(x_c) = r_{\mu\nu}[(1-x_c^2)\,\Gamma'_l(x_c)+2x_c\,\Gamma_l(x_c)], \\ \psi_g=\psi_l=0, \quad \psi'_g = r_\nu\psi'_l, \quad \Gamma_g = r_\nu\Gamma_l \quad \text{at} \quad x=x_c, \\ r_\nu = \nu_l/\nu_g, \quad r_{\mu\nu} = \rho_l\nu_l^2/\rho_g\nu_g^2. \end{array}\right\} \tag{21}$$

In absence of body forces, $f_r = f_\theta \equiv 0$, (12) can be integrated once (Sozou 1992)

$$(1-x^2)\,F''+2xF'-2F = \Gamma^2. \tag{22}$$

The integration constant is zero due to (6) and (14) and similar conditions at $x=-1$.

Thus, we have to integrate the system (3), (13) and (22) in both the regions $-1 \leqslant x < x_c$ and $x_c < x \leqslant 1$ satisfying (21),

$$\psi_g = \Gamma_g = 0 \quad \text{at} \quad x=-1, \qquad \psi_l = \Gamma_l = 0 \quad \text{at} \quad x = 1, \tag{23}$$

and condition (10) for the liquid flow.

3.2. *Collapse*

Since the existence of collapse is a sufficient condition for the swirl dynamo to occur in cones with $x_c > 0$, it is useful to show first how the forcing intensity, at which the collapse occurs, depends on the cone angle. In the case of the surface forcing, this relation can be explicitly expressed in terms of elementary functions. Without swirl and body forces, the right-hand side of (12) is zero, and $F = C(1-x)^2$ in accordance with (14). Then (13) has an analytical solution (Yatseev 1950; Squire 1952). In the region $x_c \leqslant x \leqslant 1$, this solution satisfying (7) is

$$\psi = 2\lambda(1-x)\,[(1+x)^n-(1+x_c)^n]/[a-(1+x)^n] \quad \text{for} \quad C<1/2, \tag{24a}$$

$$\psi = (1-x)/\{2/\ln[(1+x)/(1+x_c)]-1\} \quad \text{for} \quad C=1/2, \tag{24b}$$

$$\psi = 2C(1-x)/\{\omega\cot(\tfrac{1}{2}\omega\ln[(1+x)/(1+x_c)])-1\} \quad \text{for} \quad C>1/2. \tag{24c}$$

Here $\lambda = (1+n)/2$, $a = (1+x_c)^n(1+n)/(1-n)$, $\omega = \mathrm{i}n$, $n = (1-2C)^{1/2}$; and constant C relates to the Reynolds numbers:

$$Re = C(1-x_c)/(1+x_c) \quad \text{and} \quad Re_\tau = 2Re\,[(1+x_c)/(1-x_c)]^{1/2}, \tag{25}$$

where $Re = -rv_{rc}/\nu = \psi'(x_c)$ is the Reynolds number based on the radial velocity at the cone surface v_{rc}, and is a more convenient characteristic of the flow. (If subscripts g and l are not used, this means that quantities are based on liquid characteristics.) Again, the minus sign is used to make Re positive when v_{rc} is negative. For the gas flow in region $-1 \leqslant x \leqslant x_c$, the solution follows from (24) after the transformation: $x \to -x$ and $x_c \to -x_c$.

The collapse occurs when the denominators in (24) become zero at $x = 1$. When $C = 1/2$, it follows from (24*b*) and (25) that at $x_c = 2/\mathrm{e}^2-1 = x_1 \approx -0.73$,

$$Re^* = (\mathrm{e}^2-1)/2 \approx 3.19 \quad \text{and} \quad Re^*_\tau = (\mathrm{e}^2-1)^{1/2},$$

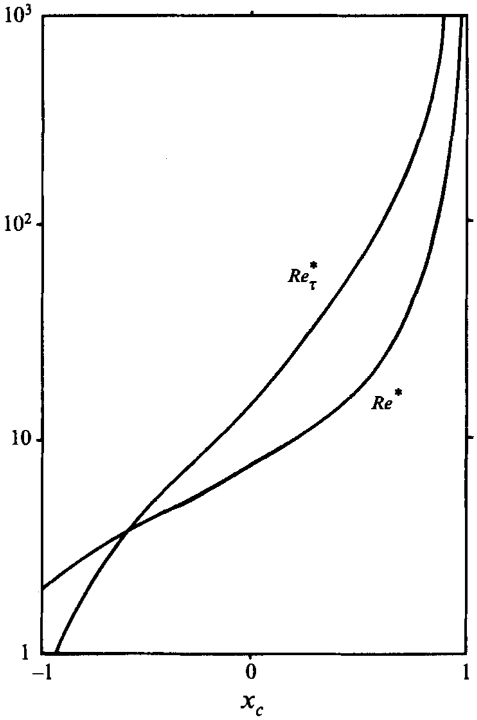

FIGURE 4. The collapse values of Re^*_τ and Re^* versus the cone angle.

where superscript asterisk marks values corresponding to the collapse. For $x_c > x_1$, we have to find a root $\omega = \omega^*$ of the equation

$$\tan(b\omega) = \omega, \quad b = \tfrac{1}{2}\ln[2/(1+x_c)].$$

We need a positive ω^* that is less than $\pi/(2b)$. Since $b < 1$ at $x_c > x_1$, it is evident that such a root exists at any x_c in the interval $x_1 < x_c < 1$. Then using $C^* = (\omega^{*2}+1)/2$ in (25) we find Re^* and Re^*_τ. For $x_c < x_1$, one needs to find a positive root $\gamma = \gamma^*$ of the equation

$$\exp(-2b\gamma) = (1-\gamma)/(1+\gamma).$$

Since $b > 1$ at $x_c < x_1$, it is evident that such a root exists; it is unique, and $\gamma^* < 1$. Then applying $C^* = (1-\gamma^{*2})/2$ in (22) we find Re^* and Re^*_τ. Figure 4 shows $Re^*(x_c)$ and $Re^*_\tau(x_c)$ obtained numerically. Thus, the collapse occurs at finite values of Re and Re_τ in the whole range $-1 < x_c < 1$.

As has been shown in §2 this proves the existence of the swirl dynamo for the one-medium SSF and $0 < x_c < 1$. (See another version of the proof in Shtern *et al.* 1994.) The proof for the BFF case is given in §4.6.1.

3.3. *Linear problem*

To solve the linear problem of the swirl dynamo, one could use solution (24) for the meridional liquid flow and the corresponding solution for the gas flow. However, it is better to integrate (3), (13), and (22) from $x = x_c$ in both directions, using (21), $\Gamma_l(x_c) = 1$, and a tentative value of $\Gamma'_g(x_c)$. Then we choose $\Gamma'_g(x_c)$ to satisfy $\Gamma_g(-1) = 0$, and look for $Re_\tau = Re_{\tau*}$ (or $Re = Re_*$) to satisfy $\Gamma_l(1) = 0$.

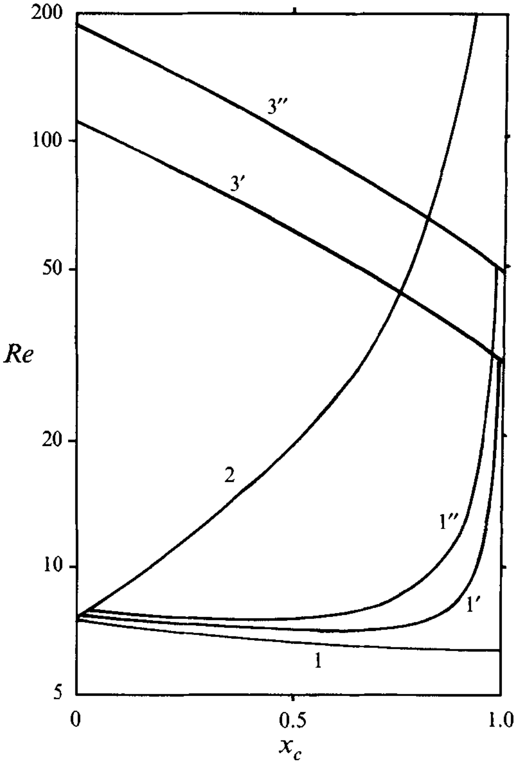

FIGURE 5. The critical Reynolds numbers (based on the liquid viscosity) of the swirl bifurcation (curves 1), collapse of the non-swirling solution in liquid (curve 2) and gas (curves 3) in the two-medium problem with water–CO_2 (prime), heptane–air (double prime), and infinite liquid/gas density ratio (curve 1).

In our calculations we use the reference temperature 20 °C for densities and viscosities and consider water ($\nu_l = 1.01 \times 10^{-6}$ m^2 s^{-1}, $\rho_l = 997$ kg m^{-3}) and heptane ($\nu_l = 0.611 \times 10^{-6}$ m^2 s^{-1}, $\rho_l = 684$ kg m^{-3}) as the liquids, and CO_2 ($\nu_g = 15 \times 10^{-6}$ m^2 s^{-1}, $\rho_g = 1.84$ kg m^{-3}) and air ($\nu_g = 14.8 \times 10^{-6}$ m^2 s^{-1}, $\rho_g = 1.21$ kg m^{-3}) as the gases.

Figure 5 shows the results of the calculations for this linear problem of the swirl dynamo. Curve 1 shows $Re_*(x_c)$ for the swirl bifurcation in the one-medium case. Curve 1 is the limit (as $r_{\mu\nu} \rightarrow \infty$) for the similar curve in the two-medium problem. The latter case correspond to curves 1′ (water–CO_2, $r_\nu = 0.067$, $r_{\mu\nu} = 3.84$) and 1″ (heptane–air, $r_\nu = 0.0413$, $r_{\mu\nu} = 0.964$). Curve 2 shows $Re^*(x_c)$ for the collapse in the liquid flow. The collapse values of $Re^*(x_c)$ for gas flows are shown by curves 3′ (CO_2) and 3″ (air) with Re^* based on water (3′) and heptane (3″) viscosities. At $r_\nu = 1$, curves 3′ and 3″ would just be reflections of the curve for Re^* in figure 4 with respect to the line $x_c = 0$. As r_ν decreases, curves 3′ and 3″ shift up in figure 5. Bifurcation curves 1′ and 1″ terminate when they meet curve 2 at small x_c (≈ 0.01 and 0.02 respectively) and curves 3′ and 3″ at x_c close to 1 (0.991 and 0.989 respectively).

Although the range of the cone angle where the swirl bifurcation occurs decreases slightly in the two-medium cases in comparison with that for the one-medium problem, this range stays wide enough to cover the experimental interval, $32° < \theta_c < 46°$. (Although Taylor predicted $\theta_c = 49.3°$ for the iso-potential surface of highly conducting liquids at rest, the experimental range for electrosprays is different due to

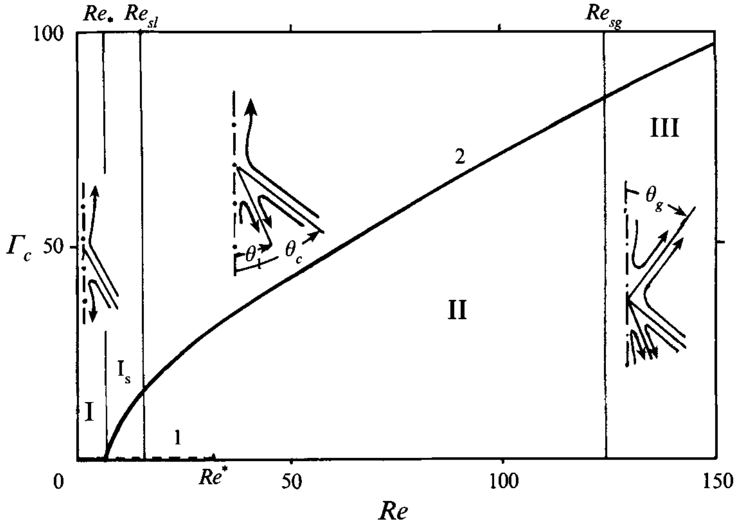

FIGURE 6. Circulation at the interface Γ_c versus the Reynolds number Re for the primary (curve 1) and secondary (curve 2) solutions. Re_*, Re_{sl}, Re_l^*, and Re_{sg} correspond to the swirl bifurcation, flow separation in liquid, collapse of the liquid flow, and flow separation in gas, respectively. The sketches illustrate flow patterns of the meridional motion in regions I (without swirl), I_s (with swirl but without separation), II (after separation in liquid), and III (after separation in gas). Water–CO_2, $\theta_c = 45°$.

emission of charges (Fernandez de la Mora 1992; Pantano, Gañan & Barrero 1994).) Inside the experimental range, the difference in Re_* is not too large for the two- and one-medium cases.

3.4. *Nonlinear problem*

To solve the nonlinear problem of the swirl dynamo, we apply the same algorithm as in §3.3 but instead of the use of normalization condition, $\Gamma_l(x_c) = 1$, we consider $\Gamma_l(x_c)$ as a free parameter. Since nonlinear results coincide with linear one as $\Gamma_l(x_c) \to 0$, we start from a small value of $\Gamma_l(x_c)$ and increase it gradually using the previous results as initial guesses for the parameters in the Newton shooting procedure.

Figures 6–8 summarize the calculation results for the water–CO_2 case. Figure 6 shows at $\theta_c = 45°$ the dependence of $\Gamma_c = \Gamma(x_c)$ on Re (curve 2). Line 1 (on the abscissa) corresponds to the primary solution, $\Gamma_c = 0$. It is shown by a dashed line for $Re > Re_* = 6.92$ because we expect it to become unstable after bifurcation. Line 1 terminates at $Re = Re^* = 31.6$ where the collapse occurs. As the abscissa in figure 6 is the line of symmetry, one has the supercritical pitchfork bifurcation of the secondary regime. We have found that the bifurcation is supercritical for all parameter values considered.

Figure 7 shows a general regime map for all values of the interface angle θ_c. As expected, the self-swirling regimes exist only in the range $0 < x_c < 1$. Figure 7(*b*) covers this range, and figures 7(*a*) and 7(*c*) show the blown-up vicinities of $x_c = 0$ and $x_c = 1$, respectively. Region I (at small Re) corresponds to the swirl-free regimes (for a typical flow pattern see the sketch in region I of figure 6). At curve B, bifurcation of swirl occurs but the pattern of the meridional flow in region I_s remains the same as in region I. Curve B terminates at the intersection points with curves C_l and C_g. The latter curves relate to the collapse in the liquid and gas flows, respectively: the lower branches correspond to collapse in the swirl-free regimes, and the upper branches correspond to the collapse in the secondary (self-swirling) regimes.

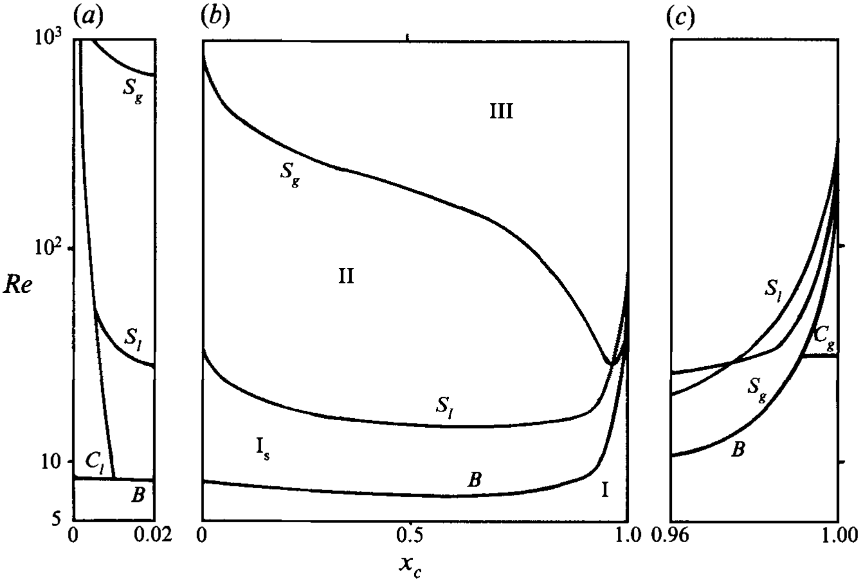

FIGURE 7. The critical Reynolds numbers (based on the water viscosity) versus the meniscus angle in the water–CO_2 case. The curves correspond to the swirl bifurcation (B), collapse in liquid (C_l) and gas (C_g) in the primary (lower branches) and secondary (upper branches) regimes, separation in liquid (S_l) and gas (S_g). (a) and (c) The blown-up vicinities of $x_c = 0$ and 1 in (b). For sketches of flow patterns in regions I, I_s, II, and III see figure 6.

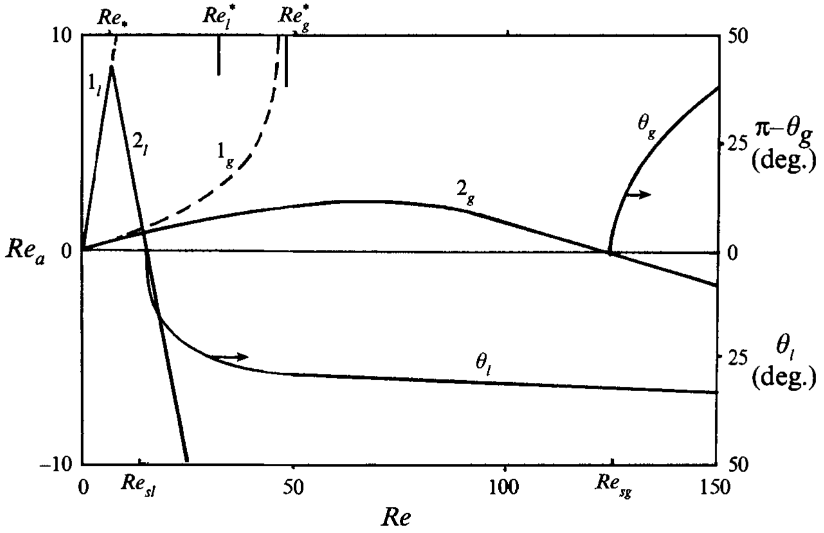

FIGURE 8. Axial velocity Re_a and separation angles θ_l and θ_g versus Re for the same problem as figure 6. Subscripts marks the values for liquid (l) and gas (g) and Re_g^* corresponds to the collapse of non-swirling gas flow; for the other symbols see figure 6.

The self-generated swirl decreases the axial velocity in comparison with the primary non-swirling regime, as figure 8 shows at $\theta_c = 45°$. Defining $Re_a = rv_{ra}/\nu$, where v_{ra} is the axial velocity, curves 1_l and 1_g correspond to Re_a for the primary regimes in the liquid and gas respectively. The vertical lines, $Re = Re_l^*$ and $Re = Re_g^*$, are asymptotes related to the collapse of the swirl-free flows of the liquid and gas, respectively. For the secondary regimes, the axial velocity of the gas (curve 2_g) is less than that for the primary regime, but continues to increase with *Re* in some range after the swirl bifurcation. In contrast, the axial velocity of the liquid (curve 2_l) begins to decrease immediately after the bifurcation. This means that the meridional motion near the axis uses its energy for swirl generation. In turn, swirl makes the near-axis jet wider and weaker owing to the centrifugal force action. As swirl increases, this action leads to another qualitative change in the flow pattern.

3.5. *Flow separation*

The axial velocity (i.e. Re_a) changes its sign at $Re = Re_{sl} = 14.3$, which corresponds to the crossing of line $Re_a = 0$ by curve 2_l in figure 8. This means that there is internal flow separation, i.e. near the axis of the liquid meniscus a new circulation cell of angle θ_l appears. Curve θ_l in figure 8 shows the dependence of the separation angle on *Re*, and the sketch in region II of figure 6 illustrates a typical flow pattern. As *Re* increases beyond 59 in figure 8, the axial velocity of the gas also begins to decrease and changes its sign at $Re = Re_{sg} = 124$. This means that internal separation also occurs in the gas flow and a new circulation cell appears within the interval $\theta_g < \theta < \pi$. Curve θ_g in figure 8 shows the dependence of the separation angle in the gas flow on *Re*, and the sketch in region III of figure 6 illustrates a typical flow pattern. Thus, the meridional motion has a four-cell pattern at high *Re*.

In figure 7 curves S_l and S_g show the dependence of Re_{sl} and Re_{sg} on x_c. Figure 7(*c*) shows that flow separation occurs first in the gas as *Re* increases. However, this is valid only for very sharp liquid menisci outside the range of the cone angles observed in electrosprays. As x_c tends to 0 and 1, $Re \to \infty$ along S_l and S_g, and these curves approach asymptotically the upper branches of C_l (as $x_c \to 0$) and C_g (as $x_c \to 1$). For large *Re*, the solution can be obtained analytically by applying an asymptotic technique.

3.6. *Asymptotic study*

Studying the flow features at high *Re*, we use a technique similar to that in Paull & Pillow (1985) for $x_c = 1$, in Shtern & Hussain (1993) for $x_c = 0$ and in Shtern & Hussain (1995) for arbitrary x_c. Here the difference is in the boundary conditions at $x = x_c$ and that we study the two-medium case as well. First, we consider the case when Γ_c, $x_{sl} = \cos(\theta_l)$ and $x_{sg} = \cos(\theta_g)$ are given and independent. Then we find a relation between them induced by the continuity requirement at $x = x_c$ yielding the final formulae for the asymptotic relations. We suppose, as is usual, that as $Re \to \infty$ the flow contains regions of inviscid behaviour and thin layers where the role of viscosity cannot be ignored. Our asymptotic analysis consists of finding analytical solutions for the inviscid regions, analytical or numerical solutions for viscous layers, and matching the solutions at the region boundaries.

3.6.1. *Inviscid regions*

Referring readers to Shtern & Hussain (1993, 1995) for details of the asymptotic technique and omitting calculations we show just the results. The circulation is a step function of x:

$$\begin{array}{llll} \Gamma_g \equiv 0 & \text{at} & -1 \leqslant x \leqslant x_{sg} & \text{(region 1)}, \\ \Gamma_g \equiv r_v \Gamma_c & \text{at} & x_{sg} \leqslant x \leqslant x_c & \text{(region 2)}, \\ \Gamma_l \equiv \Gamma_c & \text{at} & x_c \leqslant x \leqslant x_{sl} & \text{(region 3)}, \\ \Gamma_l \equiv 0 & \text{at} & x_{sl} \leqslant x \leqslant 1 & \text{(region 4)}. \end{array}$$

The analytical solution for the stream function is

$$\psi_g = \psi_{sg}(1+x)/(1+x_{sg}), \qquad \text{(region 1)},$$
$$\psi_g = -\psi_{sg}\{(x_c-x)\,[(x_c-x_{sg})\,(1+x)+(x-x_{sg})\,(1+x_c)]\}^{1/2}/c_{sg}, \qquad \text{(region 2)},$$
$$\psi_l = \psi_{sl}\{(x-x_c)\,[(x_{sl}-x_c)\,(1-x)+(x_{sl}-x)\,(1-x_c)]\}^{1/2}/c_{sl}, \qquad \text{(region 3)},$$
$$\psi_l = -\psi_{sl}(1-x)/(1-x_{sl}), \qquad \text{(region 4)},$$

where

$$c_{sg} = (x_c-x_{sg})\,(1+x_{sg})^{1/2}, \quad \psi_{sg} = r_\nu \Gamma_c c_{sg}(1+x_c)^{-1}\,(1-x_{sg})^{-1/2},$$
$$c_{sl} = (x_{sl}-x_c)\,(1-x_{sl})^{1/2}, \quad \psi_{sl} = c_{sl}\Gamma_c(1-x_c)^{-1}\,(1+x_{sl})^{-1/2}.$$

As the vorticity components for the conical flows are

$$\omega_r = -\nu r^{-2}\,\Gamma'(x), \quad \omega_\theta = 0, \quad \omega_\phi = -\nu r^{-2}\,\psi''(x),$$

one can see that the inviscid flow is potential in regions 1 and 4 but vortical in regions 2 and 3.

3.6.2. *Viscous jets inside the media*

There are jumps in the above inviscid solutions for the circulation and stream function at $x = x_{sg}$ and $x = x_{sl}$. This means that there are thin layers where viscous effects cannot be ignored. To study these boundary layers we 'blow up' the vicinities of $x = x_{sg}$ and $x = x_{sl}$ introducing the inner variables

$$\xi_g = \psi_{sg}(x-x_{sg})/[2(1-x_{sg}^2)] \quad \text{and} \quad \xi_l = \psi_{sl}(x-x_{sl})/[2(1-x_{sl}^2)],$$

and derive boundary-layer equations allowing $\Gamma_c \to \infty$. The analytical solutions of these equations are

$$\psi_g = -\psi_{sg}\tanh\xi_g, \qquad \psi_l = -\psi_{sl}\tanh\xi_l,$$
$$\Gamma_g = r_\nu\Gamma_c(1+\tanh\xi_g)/2, \qquad \Gamma_l = \Gamma_c(1-\tanh\xi_l)/2.$$

Since the circulation is a step function in the inviscid limit, the above boundary-layer solution provides a uniform approximation for the circulation in the whole interval $-1 \leqslant x \leqslant 1$. The boundary-layer solutions for the stream function are valid only in the vicinities of $x = x_{sg}$ and $x = x_{sl}$ and match the inviscid solutions as ξ_g and ξ_l tends to $\pm\infty$.

3.6.3. *Near-interface viscous layers*

Near the interface, we apply the inner variables

$$\eta = \alpha(x-x_c), \quad \psi = \alpha(1-x_c^2)\,W(\eta),$$

where scale α is different for the gas and liquid flows:

$$\alpha_g = -\psi_{sg}^{2/3}[(x_c-x_{sg})\,(1-x_c^2)\,(1-x_c)\,(1+x_{sg})]^{-1/3},$$
$$\alpha_l = \psi_{sl}^{2/3}[(x_{sl}-x_c)\,(1-x_c^2)\,(1+x_c)\,(1-x_{sl})]^{-1/3}.$$

However the resulting boundary-layer equation is universal for both media:

$$\mathrm{d}W/\mathrm{d}\eta = W^2/2-\eta+\eta_c,$$

where
$$\eta_c = \psi_g'(x_c)/[\alpha_g^2(1-x_c^2)] = \psi_l'(x_c)/[\alpha_l^2(1-x_c^2)].$$

We expect that η_c is a finite non-zero number that must be found to match the boundary-layer and outer solutions. The corresponding boundary-layer solution was found in Goldshtik & Shtern (1990) with $\eta_c = 1.28$.

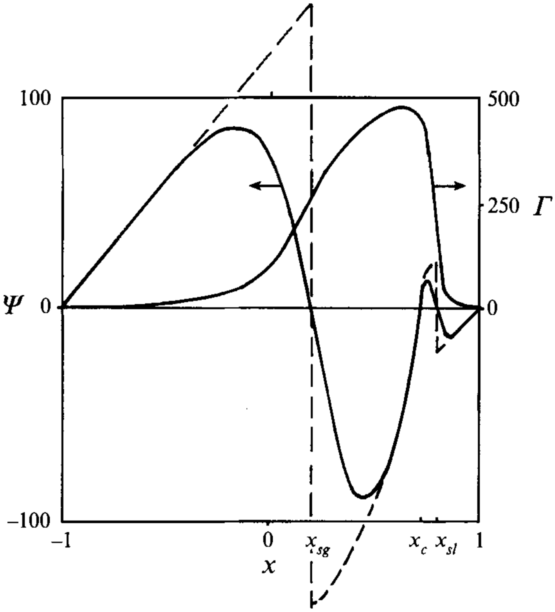

FIGURE 9. Profiles of stream function ψ and circulation Γ for the water–CO$_2$ case at $Re = 1000$ and $x_c = 0.707$ ($x_{sg} = 0.192$ and $x_{sl} = 0.781$). The dashed lines show the inviscid asymptote for ψ.

The continuity requirements at $x = x_c$ yield the relations

$$\left.\begin{aligned} &r_\mu \psi_{sl}(1-x_{sl}^2)^{-1}\operatorname{sech}^2\xi_{lc} + \psi_{sg}(1-x_{sg}^2)^{-1}\operatorname{sech}^2\xi_{gc} = 8(r_\mu - 1)\,x_c(1-x_c^2)^{-1},\\ &(x_{sl}-x_c)/(x_c-x_{sg}) = r_\nu^{1/2}\{(1-x_c)(1+x_{sl})/[(1+x_c)(1-x_{sg})]\},\end{aligned}\right\} \quad (26)$$

where $r_\mu = r_{\mu\nu}/r_\nu$, $\xi_{lc} = \xi_l(x_c)$, and $\xi_{gc} = \xi_g(x_c)$. The expression inside the curly brackets in (26) tends to 1 as $\Gamma_c \to \infty$ because $x_{sl} \to x_c$ and $x_{sg} \to x_c$. However, the latter limit is reached rather slowly and we use (26) below in comparing our asymptotic and numerical results.

Now we have the necessary conditions to find all the parameters at given Γ_c, x_c, and the medium characteristics.

3.6.4. *Comparison of the asymptotic and numerical results*

The asymptotic and numerical solutions have been calculated for the water–CO$_2$ case at $x_c = 0.707$ and $\Gamma_c = 460$. Figure 9 shows the numerical results (solid curves) and the inviscid solution (dashed lines) for the stream function and circulation. The positions of x_{sg} and x_{sl} as well as the circulation distributions coincide within the accuracy of the drawing for the numerical and asymptotic data. A similar merging of the results for the stream function occurs when we use the products of the boundary-layer and inviscid solutions. This agreement verifies both the asymptotic and numerical results.

We mentioned that $x_{sl} \to x_c$ and $x_{sg} \to x_c$ as $\Gamma_c \to \infty$ and therefore the viscous jets positioned inside the media approach the interface. However, the jets and the near-surface boundary layer do not merge. There are regions of the inviscid vortical flows in between, although the thickness of these regions tends to zero as $\Gamma_c \to \infty$. The reason for this is that the thickness of the boundary layers tends to zero faster than that of the inviscid regions.

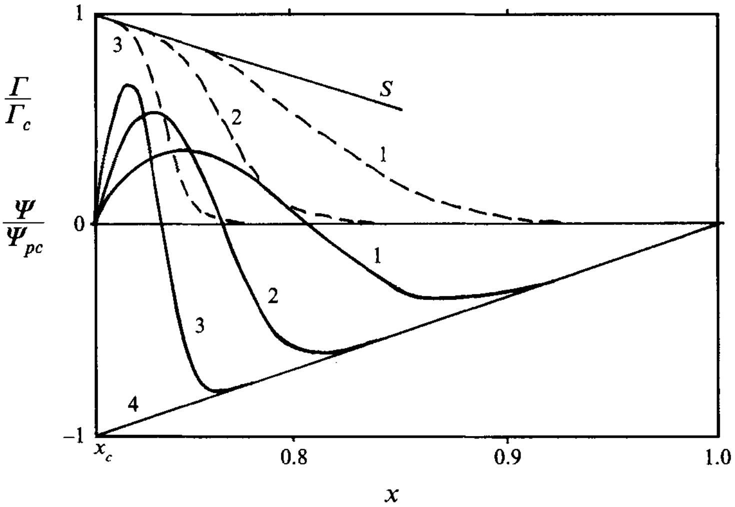

FIGURE 10. Distributions of stream functions (solid curves) and circulation (dashed curves) at $\Gamma_c =$ 200 (curve 1), 800 (curve 2), and 3200 (curve 3). Line 4 shows the potential limit of $\psi(x)$ as $\Gamma_c \to \infty$, line S shows the slope of $\Gamma(x)/\Gamma_c$ at $x = x_c = 0.707$.

Figure 10 illustrates the development of the flow structure (as Γ_c increases) for the one-medium case with the included angle of the meniscus $\theta_c = 45°$. Distributions of the stream function (solid curves) and circulation (dashed curves) are shown for $\Gamma_c = 200$, 800, and 3200 ($Re = 370$, 1869, and 8677). Line S shows the slope of circulation on the cone surface according to (11). One can see that the separation position $x = x_s$ (zero of ψ) moves to the surface as Re increases. In other words, the inner cell becomes wider and the angular thickness of the outer cell tends to zero as $Re \to \infty$. The swirl is concentrated near the surface and is absent outside a thin near-surface layer. Inside the inner cell, the stream function tends to the linear distribution $\psi_p(x) = \psi_{pc}(1-x)/(1-x_c)$, $\psi_{pc} = \psi_p(x_c)$, corresponding to a potential flow (see above) and shown by line 4 in figure 10. The different signs of $\psi'(x_c)$ and $\psi'(x_s)$ correspond to the oppositely directed viscous jets near $x = x_c$ (inflow) and $x = x_s$ (outflow).

Thus, the asymptotic analysis together with the numerical results allow us to cover the whole range of Re values – from zero to infinity. Both in the one- and two-medium problem, bifurcation of the self-swirling regimes and flow separations occur as the intensity of swirl becomes sufficiently large. Asymptotically, the rotation is present only in a thin recirculation cells near the interface, where strong in- and outflows also develop. This asymptotical flow structure differs drastically from that in the case of body forcing that we study below.

4. Body forcing

4.1. *Modification of the problem*

Now we consider the case when the meridional motion inside a liquid cone is driven by body electric forces. Following Sozou (1971) and Sozou & Pickering (1976) we neglect the influence of the flow on the electric field. This is valid if the Batchelor number β (that is the kinematic/magnetic viscosity ratio) is significantly less than 1. This is the case for many applications, e.g. for mercury $\beta = 10^{-7}$ (Bojarevics *et al.* 1989).

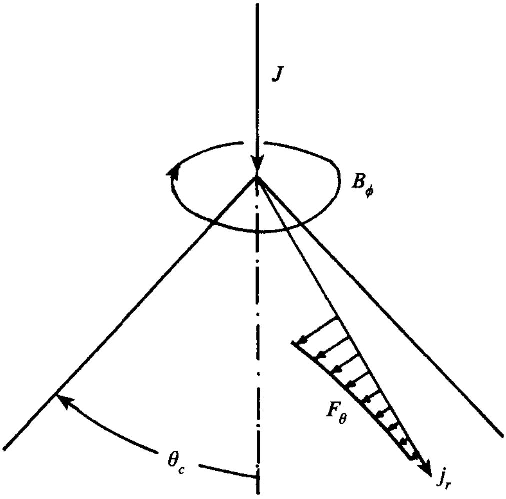

FIGURE 11. Schematic of the radial distribution of body force F_θ induced by the vector product of the electric current density j_r and magnetic induction B_ϕ (see also figure 2*b*).

Figure 11 shows a schematic of the forcing. Electric current J diverges radially from the cone apex to infinity with the density

$$j_r = J/[2\pi r^2(1-x_c)],$$

and generates the azimuthal magnetic field B_ϕ which, from $\nabla \times \boldsymbol{B} = 4\pi \boldsymbol{j}$, is given by

$$B_\phi = 2J[r(1-x_c)]^{-1}[(1-x)/(1+x)]^{1/2}.$$

Since the electromagnetic force $\boldsymbol{F} = \boldsymbol{j} \times \boldsymbol{B}$, this force acts along meridians, and

$$F_\theta = -J^2[\pi r^3(1-x_c)^2]^{-1}[(1-x)/(1+x)]^{1/2}. \tag{27}$$

It is convenient to introduce the dimensionless total current $I = J(\pi\rho\nu^2/2)^{-1/2}$. ($I = K^{1/2}$, where K is the parameter used by Sozou 1971.) Then it follows from (1) and (27) that

$$f_\theta = -\tfrac{1}{2}I^2(1-x_c)^{-2}[(1-x)/(1+x)]^{1/2}. \tag{28}$$

Substituting (28) in (12) and taking into account that $f_r \equiv 0$, we have

$$(1-x^2)F''' = 2\Gamma\Gamma' + I^2(1-x)(1-x_c)^{-2}. \tag{29}$$

Thus, now the governing equations are (3), (13) and (29). The boundary conditions at the axis continue to be (4)–(6), leading to (14). At the cone surface we apply (7) and

$$\psi''(x_c) = 0, \tag{30}$$

which corresponds to zero radial shear stresses and follows from (10) when $Re_\tau = 0$.

Studying the collapse problem (which is closely related to the swirl dynamo, see §2.2) we use instead of (11) the condition

$$\Gamma(x_c) = \Gamma_c, \tag{31}$$

where Γ_c is considered as a given value that characterizes an *external forcing* of rational motion. The collapse of the flow in a half-space with a free surface at $x = 0$ and zero circulation Γ_c was studied by Sozou & Pickering (1976). We generalize this problem here for arbitrary values of x_c and Γ_c.

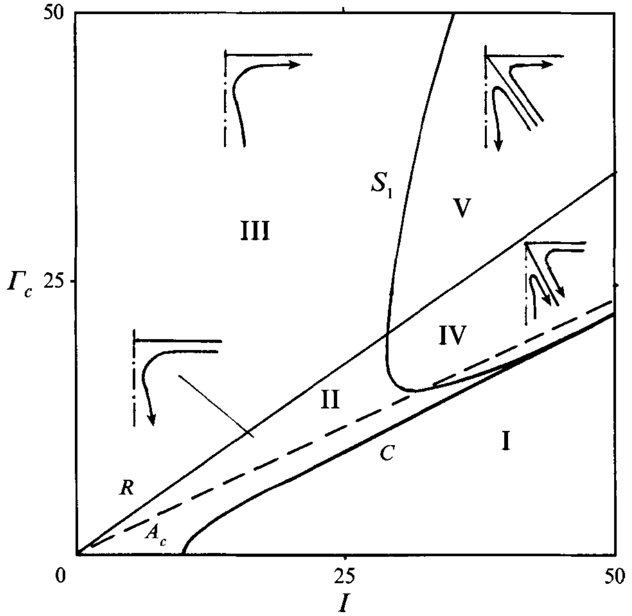

FIGURE 12. Regime map for a flow in a half-space driven by the body forces induced by current I (dimensionless) and circulation Γ_c applied at the surface. The curves correspond to no meridional motion (R), collapse (C and its asymptote A_c), and the first separation (S_1). There is no regular solution in region I, and the sketches show flow patterns in regions II–V.

The main advantage of using (29) is that this equation can be integrated analytically in important particular cases. Note that (7), (15), and (30) yield

$$F'(x_c) = 0, \tag{32}$$

which, together with (14), means that the boundary conditions for F admit a solution $F \equiv 0$. A solution of (29) has to be non-zero, therefore, owing to the right-hand side terms. Since (29) is linear with respect to F, we can use the decomposition

$$F = \Gamma_c^2 F_\Gamma + I^2 F_J, \tag{33}$$

where $\Gamma_c^2 F_\Gamma$ and $I^2 F_J$ are contributions from the first and second terms on the right-hand side of (29), respectively.

The explicit form of F_J, which follows from integration of (29) at $\Gamma \equiv 0$ and $I^2 = 1$ with conditions (14) and (32), is

$$F_J = \frac{1}{2(1-x_c)^2}\left[(1+x)^2 \ln\frac{1+x}{2} + 2 - 2x + \left(\frac{1+x_c}{1-x_c}\ln\frac{1+x_c}{2} - \frac{1}{2}\right)(1-x)^2\right]. \tag{34}$$

Also, the integral form of F_Γ, which follows from integrating (29) three times and applying conditions (14) and (32) at $I^2 = 0$, is

$$F_\Gamma = \frac{(1-x)(2x_c - x - 1)}{4(1-x_c)} - \tfrac{1}{2}(\gamma^2 - 1)\frac{1+x}{1-x} + (1-x)^2 \int_{x_c}^{x} \gamma\gamma' \frac{\mathrm{d}t}{1-t^2}$$
$$- \frac{(1-x^2)}{2(1-x_c)} \int_{x_c}^{1} (\gamma^2 - 1)\frac{\mathrm{d}t}{(1-t)^2} - x\int_{x}^{1} (\gamma^2 - 1)\frac{\mathrm{d}t}{(1-t)^2}, \tag{35}$$

where $\gamma = \Gamma/\Gamma_c$.

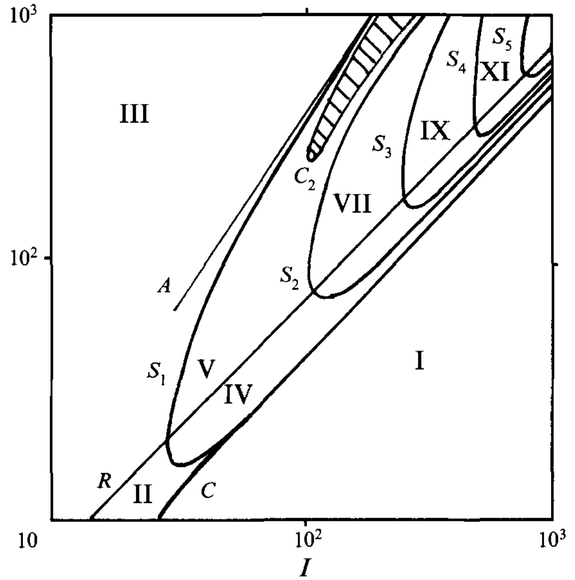

FIGURE 13. As figure 12 but for larger I and Γ_c. Line A is an asymptote for S_1, curves S_2–S_5 correspond to subsequent flow separations, and curve C_2 corresponds to the collapse in the two-cell flow. In regions VII, IX, and XI, the flow is 3-, 4-, and 5-cellular, respectively.

4.2. *Collapse in the one-cell flow*

When collapse occurs in the one-cell flow, the circulation becomes constant, i.e. $\Gamma \equiv \Gamma_c$ in $x_c \leqslant x < 1$. Substitution of $\gamma \equiv 1$ in (35) makes all terms on the right-hand size zero except for the first one. Therefore, in the collapse case, it follows that

$$F_\Gamma = F_\Gamma^* = -\tfrac{1}{4}(1-x)(1+x-2x_c)/(1-x_c), \tag{36}$$

and the problem is reduced to integration of (13) with

$$F = F^* = \Gamma_c^2 F_\Gamma^* + I^2 F_J, \tag{37}$$

and the condition $\psi(1) = 4$ (for the latter see Goldshtik & Shtern 1989). It follows from (15), (36) and (37) that $\psi'(1) = 2 - \Gamma_c^2/8$. In our numerical calculations, we perform the integration from $x = 1$ to $x = x_c$ and choose $I = I^*$ at given Γ_c to satisfy (7).

For large Γ_c, the asymptotic collapse relation between I^* and Γ_c can be found analytically. In this case $F = -\tfrac{1}{2}\psi^2$ becomes valid for the inviscid solution, and to satisfy (7) we need $F(x_c) = 0$. Then it follows, from substitution of $x = x_c$ into (36) and (37), that

$$I^* = \tfrac{1}{2}\Gamma_c[(1-x_c)/F_J(x_c)]^{1/2}. \tag{38}$$

The collapse relation $I^*(\Gamma_c)$ calculated numerically at $x_c = 0$ is shown by curve C in figures 12 and 13. The asymptote (38), that is reduced to $I^* = \Gamma_c(3-4\ln 2)^{-1/2} \approx 2.1\Gamma_c$ at $x_c = 0$, is shown by line A_c in figure 12 and coincides within the accuracy of the drawing with curve C in figure 13 for $\Gamma_c > 100$.

Thus, circulation applied at the surface increases the critical value of the electric current corresponding to the collapse. The reason is that the circulation generates negative F_Γ (see e.g. (36)), i.e. induces meridional motion *diverging* from the symmetry axis contrary to the current action that induces *converging-to-axis* flow. In particular, the circulation reduces the axial velocity, and a larger value of I is needed for the collapse. In the next section we show how some specially chosen Γ_c at given I can stop the meridional motion.

4.3. *Suppression of the meridional motion by swirl*

This effect can be useful in some applications, such as electroslag welding (Bojarevics *et al.* 1989). A meridional motion in the latter leads to non-uniformity of crystal growth, so it is useful to suppress the motion. As further motivation, the self-rotation is closely related to the suppression effect, as shown below.

Suppose that meridional motion is absent, i.e. $\psi \equiv 0$. Then (3), (6), and (31) yield

$$\Gamma = \Gamma_c(1-x)/(1-x_c), \tag{39}$$

and substituting (39) into (29) gives

$$(1-x^2)F''' = (I^2-2\Gamma_c^2)(1-x)(1-x_c)^{-2}. \tag{40}$$

Therefore at

$$\Gamma_c = \Gamma_R = I/\sqrt{2} \tag{41}$$

the right-hand side of (40) becomes zero, which on using (14) and (32) leads to $F \equiv 0$, and hence, with use of (7) and (13), that $\psi \equiv 0$. Note that condition (41) is valid for any given I and does not depend on the cone angle. The relation is presented by ray R in figures 12 and 13. In a more general case, the opposite actions of the current and circulation do not totally stop the meridional motion but lead to a cascade of flow separations and multi-cell flow patterns.

4.4. *Separation*

4.4.1. *The first separation*

Figure 12 shows a map of flow regimes at moderate values of I and Γ_c. The meridional motion does not depend on the circulation sign and the current direction, so that the abscissa, $\Gamma_c = 0$, and the ordinate, $I = 0$, are symmetry lines. Besides curve C and lines R and A_c which have been mentioned above, there is curve S_1 on which the axial velocity changes its sign. The parameter plane in figure 12 is subdivided into regions I–V separated by C, S_1 and R. There is no regular solution of the problem in region I positioned below the collapse curve C. The sketches inside the other regions show typical flow patterns for the meridional motion.

Passing through R, the meridional motion changes its direction, stopping totally at R. When one crosses S_1 along the ray $\Gamma_c = aI$ as I increases, the flow becomes two-cellular, and angle θ_s of the separating cone starts from zero at S_1, monotonically grows, and tends to 90° as $I \to \infty$.

In the vicinity of R, the meridional motion is slow and the problem can be reduced to a linear one. First, note that (29) can be integrated once to give

$$(1-x^2)F''+2xF'-2F = \Gamma^2-\tfrac{1}{2}I^2(1-x)^2/(1-x_c)^2. \tag{42}$$

In the vicinity of R, the circulation can be represented by a superposition of the basic solution Γ_b and disturbance Γ_d:

$$\Gamma = \Gamma_b+\Gamma_d, \quad \Gamma_b = \Gamma_R(1-x)/(1-x_c), \quad |\Gamma_d| \ll \Gamma_b. \tag{43}$$

Substituting (43) in (42), and neglecting nonlinear terms with respect to the disturbance, we have with the help of (3) and (13)

$$\left.\begin{aligned} &(1-x^2)\Gamma_d'' = y_d\Gamma_b', \quad (1-x^2)\psi_d'+2x\psi_d = F_d, \\ &(1-x^2)F_d''+2xF_d'-2F_d = 2\Gamma_b\Gamma_d. \end{aligned}\right\} \tag{44}$$

We integrate (44) subject to the same boundary conditions (4)–(7) and (30), but instead of (31) use the normalization $\Gamma_d(x_c) = -1$. Thus a one-parameter family of solutions

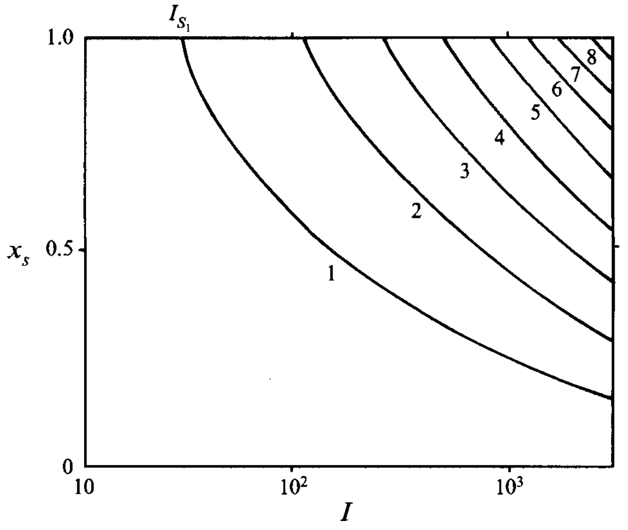

FIGURE 14. Angles of cones separating the flow cells versus current I along ray R in figure 13. The cone number (counting from the surface) is shown near the corresponding curve.

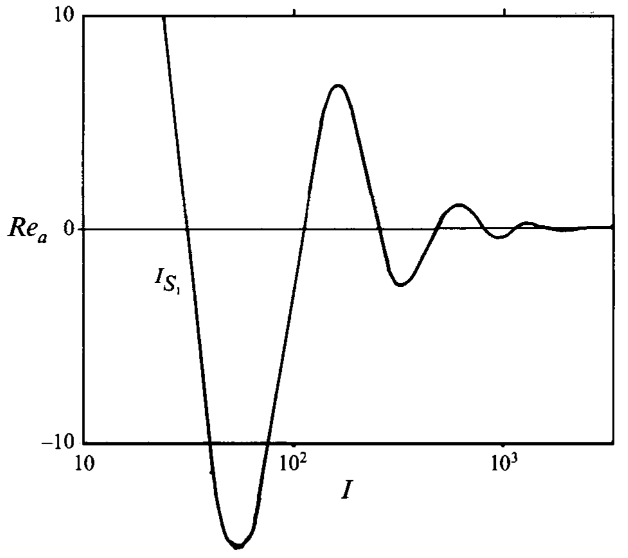

FIGURE 15. Dependence of axial velocity Re_a versus current I along ray R in figure 13. Zeros of $Re_a(I)$ correspond to the subsequent flow separations.

is obtained, depending on I. At small I, the solution corresponds to a one-cell regime, but when I becomes larger than $I_{S_1} = 28.9$ (this value relates to the intersection point of R and S_1 in figure 12), the second cell appears near the axis. Despite the fact that the meridional motion stops at R, angle θ_{S_1} of the first separating cone has a limiting value differing from 0 and 90° as one approaches R for $I > I_{S_1}$. Curve 1 in figure 14 shows the quantity $x_{S_1}(I)$ and figure 15 shows $Re_a(I)$ ($Re_a \equiv -\psi'(1)$ is a dimensionless axial velocity) along ray R in figures 12 and 13. As the condition $\Gamma_a(x_c) = -1$ corresponds to points positioned a little bit below ray R, the flow is converging to the axis at small I, and Re_a is positive. Then Re_a changes its sign at $I = I_{S_1}$, which corresponds to the origin of curve 1 at $I = I_{S_1}$ in figure 14. The relation between I_{S_1} and

Γ_c for curve S_1 in figures 12 and 13, which is not close to R, has been obtained numerically (see below), but the asymptotes of S_1 can be found analytically.

4.4.2. *Asymptotic study of the first separation*

Curve S_1 separating one- and two-cell regimes in figures 12 and 13 has two branches, and we will now find asymptotes for both branches as $I \to \infty$. The lower branch corresponds to the converging-to-axis meridional flow. As I increases, the circulation tends to Γ_c everywhere except in the vicinity of the axis where a boundary layer develops, and the inviscid limit for the stream function is the same as in the collapse case (see §4.2). Therefore, as $I \to \infty$, the leading term of the asymptotic expansion for the lower branch coincides with that for the collapse, i.e. (38). One can see in figure 13 that the lower branch of S_1 merges with curve C within the accuracy of the drawing at $I > 100$. Nevertheless, the flows are significantly different for S_1 and C in the near-axis boundary layer. The boundary layer for the near-collapse flows has been studied by Goldshtik & Shtern (1990) and their results are also valid for this problem. In this boundary-layer approach, the equations for the meridional motion decouple from those for the swirl and have a solution corresponding to the round Schlichting jet.

However, these equations stay coupled when the separation is considered, and for this case the boundary-layer problem is reduced to that formulated by Long (1961). Introducing the inner independent variable $\eta = \Gamma_c^2(1-x)$, using $\gamma = \Gamma/\Gamma_c$, substituting these variables in equations (3), (13), (42), and allowing $\Gamma_c \to \infty$, we get

$$\eta\psi' = \psi - \tfrac{1}{4}\psi^2 - \tfrac{1}{2}F, \quad \eta\gamma'' = -\tfrac{1}{2}\psi\gamma', \quad \eta F'' = F' + \tfrac{1}{2}\gamma^2, \tag{45}$$

where the prime means differentiation with respect to η. The transformation, $\eta = y^2$, $F' = 4y^3 s_0$, reduces (45) to equations (2.7)–(2.9) in (Long 1961), but system (45) seems to be simpler for analysis and numerical integration. The conditions $\psi(0) = \gamma(0) = 0$ and (45) yield $F(0) = F'(0) = 0$; but neither $\psi'(0), F''(0)$, nor $\gamma'(0)$, can be found from (45). $F''(0)$ and $\gamma'(0)$ must be chosen to satisfy the conditions at infinity: $\gamma \to 1$ and $F' \to -\frac{1}{2}$ as $\eta \to \infty$. In general $\psi'(0)$ stays a free parameter, but considering the separation case we use here $\psi'(0) = 0$.

The numerical results are in agreement with those obtained by Long (1961) and Burggraf & Foster (1977) at the specific value of Long's parameter M corresponding to zero axial velocity. Note that although Long's boundary-layer approach is quite valid for the near-axis velocity field, parameter M has no sense here. (See Shtern & Hussain 1993, 1995 on the limitations of using M as a characteristic of Long's boundary layer.)

The upper branch of curve S_1 in figures 12 and 13 corresponds to the diverging-from-axis meridional flow. Owing to this convection, the circulation tends to zero as $I \to \infty$ outside the near-surface boundary layer where the circulation rises to Γ_c. Since $\Gamma \to 0$ in the inviscid region, we can use (33) with $F_\Gamma = -A(1-x)^2$ (which follows from (29) and (14) at $I = 0$ and $\Gamma \equiv 0$), where A must be found to match the boundary-layer solution. One cannot expect that $F(x_c) = 0$ in general, and therefore $F = -\frac{1}{2}\psi^2$ yields for the inviscid outer solution that $\psi(x_c) \equiv \psi_c \neq 0$. To satisfy (7) the stream function must vary from ψ_c to zero inside the near-surface boundary layer. F is a continuous function in the inviscid limit, so inside the boundary layer one can use $F \equiv -\psi_c^2/2$ in (13). Then, introducing the inner variables

$$\psi = -\psi_c W(\eta), \quad \eta = \alpha(x - x_c), \quad \alpha = \tfrac{1}{2}\psi_c/(1-x_c^2), \tag{46}$$

and allowing $\psi_c \to \infty$, we get from (13)

$$W' = 1 - W^2, \quad W = \tanh\eta, \tag{47}$$

where the prime denotes differentiation with respect η, and to find the integration constant the condition $W(0) = 0$ has been used. Applying (46) in (3) and allowing $\psi_c \rightarrow \infty$ we get

$$\Gamma'' = -2W\Gamma'.$$

Substituting for W from (47) and integrating, with the use of conditions $\Gamma(0) = \Gamma_c$ and $\Gamma(\infty) = 0$, yields

$$\Gamma = \Gamma_c(1 - \tanh \eta). \tag{48}$$

To find how F'_Γ (in decomposition (33)) varies across the boundary layer we apply (46) and (48) in (42) at $I = 0$, and in the limit $\psi_c \rightarrow \infty$ obtain

$$\alpha^2 F''_\Gamma = (1 - \tanh \eta)^2. \tag{49}$$

Integrating (49) with the condition $F'_\Gamma(0) = 0$ we find

$$\alpha^2 F'_\Gamma = 2 \ln\{2/[1 + \exp(-2\eta)]\} - \tanh \eta. \tag{50}$$

In particular, $F'_\Gamma(\infty) = (2 \ln 2 - 1)/\alpha^2$. The matching condition for the inner and outer expansions is $(\mathrm{d}F_\Gamma/\mathrm{d}x)(x_c) = \alpha(\mathrm{d}F_\Gamma/\mathrm{d}\eta)(\infty)$ (since $\mathrm{d}/\mathrm{d}x = \alpha\, \mathrm{d}/\mathrm{d}\eta$), which yields $(\mathrm{d}F_\Gamma/\mathrm{d}x)(x_c) = (2 \ln 2 - 1)/\alpha$. Then, with the help of $F_\Gamma = -A(1-x)^2$ and (46), we obtain

$$F_\Gamma = -(2 \ln 2 - 1)(1 + x_c)(1 - x)^2/\psi_c. \tag{51}$$

Substituting (51) and (34) in (33), and using $x = x_c$ and $F(x_c) = -\psi_c^2/2$, we get the relation

$$I^2 F_J(x_c) = \Gamma_c^2 (2 \ln 2 - 1)(1 + x_c)(1 - x_c)^2/\psi_c - \psi_c^2/2, \tag{52}$$

and this defines ψ_c at given I and Γ_c. One can consider Γ_c and ψ_c as given parameters as well, in which case (52) defines I, and the analytical asymptotic solution for the one-cell flow as $\Gamma_c \rightarrow \infty$ is determined by (46)–(48), (33), (34), (51), and $F = -\psi^2/2$.

Since in the inviscid region $\psi = -(-2F)^{-1/2}$, to fulfil the separation condition, $\psi'(1) = 0$, we need $F''(1) = 0$. This gives, with the help of (33) and (51), the result

$$I^2 F''_J(1) = 2\Gamma_c^2 (2 \ln 2 - 1)(1 + x_c)/\psi_c. \tag{53}$$

It follows from (34) that

$$F''_J(1) \equiv F_{J2}(x_c) = \left(\frac{1 + x_c}{1 - x_c} \ln \frac{1 + x_c}{2} + 1\right) \bigg/ (1 - x_c)^2, \tag{54}$$

and substitution of ψ_c from (53) and (54) in (52) yields the final formula

$$\Gamma_c = I^{3/2} F_3(x_c), \tag{55}$$

where $F_3(x_c) = [(1 - x_c)^2 F_{J2}(x_c) - 2F_J(x_c)]^{1/4} \{F_{J2}(x_c)/[(4 \ln 2 - 2)(1 + x_c)]\}^{1/2}$.

At $x_c = 0$ the relation (55) becomes $\Gamma_c = 0.418\, I^{3/2}$, which is shown by line A in figure 13. Since the upper branch of S_1 clearly approaches A as $\Gamma_c \rightarrow \infty$, this means that our asymptotic and numeric analyses are matched for large Γ_c. Figure 16 supports this claim for the distributions of the stream function (curves 1, 1′, and 1″) and circulation (curve 2) also. The numerical results (for $\Gamma_c = 10^3$ at the upper branch of S_1 in figure 13) are shown by the solid curves. The numerical results for the circulation differ from (48) in the third decimal digit at worst. The numerical results for the stream function coincide within the same accuracy with (46) and (47) (curve 1″) at $x < 0.03$ and with the inviscid solution (curve 1′) at $x > 0.08$. The combination of these boundary-layer and outer solutions that serves as a uniformly valid approximation merges with the numerical solution within the accuracy of the drawing.

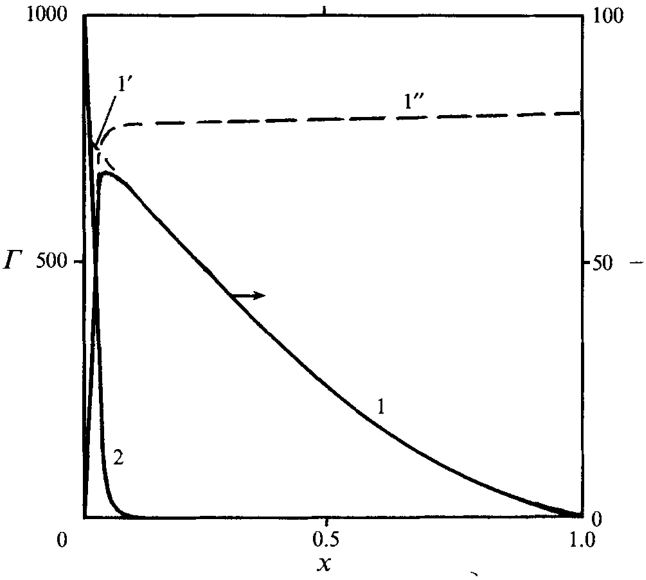

FIGURE 16. Profiles of stream function (curve 1) and circulation (curve 2) for the upper branch of S_1 in figure 13 at $\Gamma_c = 10^3$. The dashed curves show asymptotic solutions for ψ in the near-surface boundary layer (1″) and the outer inviscid region (1′). The product of (1′) and (1″) coincides with curve 1 within the accuracy of the drawing.

Note that the asymptotes for the upper, (55), and lower, (38), branches of S_1 correspond to different power-law relations between Γ_c and I. This means that at a given circulation $\Gamma_c \gg 1$, one needs a current $I \sim \Gamma_c^{2/3}$ for appearance of the converging-flow cell near the axis but a current $I \sim \Gamma_c$ to make the flow converge to the axis in the whole region. Inside these limits for I, the flow can be multi-cellular, as we will show in the next section.

4.5. *Cascade of flow separations*

4.5.1. *Linear analysis*

Let us now return to the linear system (44) that describes the flow in the vicinity of ray R in figures 12 and 13. The solution becomes oscillating, and the number of roots $x = x_{S_k}$ where $\psi(x_{S_k}) = 0$ increases as I grows (we use the following numeration of the roots: $0 \leqslant k \leqslant N, x_{S_0} = x_c$, $x_{S_k} < x_{S_{k+1}}$, and $x_{S_N} = 1$). Figure 14 shows dependencies $x_{S_k}(I)$ for $k = 1, \ldots, 8$ (the values of k mark the curves). Also figure 15 shows that the axial velocity changes its sign many times as I increases. Each zero $I = I_{S_k}$ where $Re_a = 0$ in figure 15 is a starting point for the corresponding curve in figure 14. Each interval between the adjacent curves at a fixed I in figure 14 corresponds to a separate flow cell bounded by stream surfaces $\psi = 0$. It seems from the numerical results that the number of cells tends to infinity as $I \rightarrow \infty$. The asymptotic dependence of the cell number N on I can be estimated using the high-frequency approximation of (44). For this we neglect all terms on the left-hand sides of (44) except the highest derivatives, which, together with substitution of Γ_b from (43) and (41), transform (44) to

$$(1-x^2)\,\Gamma_d'' = -a\psi_d, \quad (1-x^2)\,\psi_d' = F_d, \quad (1+x)\,F_d'' = 2a\Gamma_d,$$

where $a = I/[(1-x_c)\surd 2]$. Here, it is convenient to use θ instead of x. Then, the above system is reduced to

$$\psi_d^{\mathrm{v}} = f(\theta)\,\psi_d, \quad f(\theta) = 2a^2 \sin\theta/(1+\cos\theta), \qquad (56)$$

where ψ_d^{v} is the fifth derivative with respect to θ. Now we 'freeze' $f(\theta)$, i.e. neglect its variation between the adjacent roots, and look for a solution in the form $C\exp(\alpha\theta)$, expecting $|\alpha| \gg 1$. Substitution of this form in (56) gives

$$\alpha^5 = I^2 \frac{\sin\theta}{(1-\cos\theta)(1+\cos\theta_c)}, \quad |\alpha| = I^{2/5}\left\{\frac{\sin\theta}{(1-\cos\theta)(1+\cos\theta_c)}\right\}^{1/5}. \tag{57}$$

Since the exponent $\frac{1}{5}$ is rather small, we can replace θ by θ_c in (57) in our approximate estimations, and obtain

$$|\alpha| = I^{2/5}(\sin\theta_c)^{-1/5}. \tag{58}$$

We must consider the five complex exponents

$$\alpha_m = |\alpha|\,[\cos(2\pi m/5) + \mathrm{i}\sin(2\pi m/5)], \quad m = 1, \dots, 5,$$

and the appropriate solution, growing with θ and satisfying (7), is

$$\psi = C\exp[\alpha_r(\theta-\theta_c)]\sin[\alpha_i(\theta-\theta_c)],$$

where

$$\alpha_r = |\alpha|\cos(2\pi/5) \quad \text{and} \quad \alpha_i = |\alpha|\sin(2\pi/5). \tag{59}$$

Note that (59) must be corrected in the vicinity of $\theta = 0$ to satisfy (4), but since α_r tends to infinity with I, ψ becomes exponentially small near $\theta = 0$ in comparison with its characteristic value near $\theta = \theta_c$, so the correction is not significant.

Since the number of cells $N \approx \alpha_i\theta_c/\pi$, it follows from (58) and (59) that

$$N \approx I^{2/5}(\sin\theta_c)^{-1/5}\sin(2\pi/5)\,\theta_c/\pi. \tag{60}$$

Therefore, there is indeed an infinite sequence of flow separation as $I \to \infty$. Also, it follows from this analysis that the curves in figure 14 approach the abscissa as $I \to \infty$ with the asymptotic behaviour $x_{S_k} \sim I^{2/5}$.

4.5.2. *Nonlinear results*

Outside the vicinity of ray R in figure 13, curves S_2–S_5 (corresponding to the subsequent separations) have been obtained numerically. Like S_1, these curves have two branches with asymptotes which are parallel to the asymptotes of S_1. The reason is that the number of stream function roots is fixed along these curves, and each x_{S_k} (in particular, $x_{S_{N-1}}$) tends to some limiting value less than 1. Also $\Gamma(x_{S_k})$ tends to a limiting value less than Γ_c. Therefore, for the near-axis cell, one can apply the asymptotic results of §4.4.2 simply through replacing x_c by $x_{S_{N-1}}$ and Γ_c by the limiting value of $\Gamma(x_{S_k})$. For example, x_{S_1} tends to 0.59 and 0.64 along the upper and lower branches of S_2, respectively, as $I \to \infty$. Figure 17 shows the distributions of stream function and circulation at $\Gamma_c = 500$ for the upper branch of S_2 in figure 13. In contrast with figure 16, there are two viscous layers – near the surface and near the axis. In the near-surface layer, the circulation drops from $\Gamma = \Gamma_c$ to $\Gamma \approx 31$, then Γ stays quasi-constant inside the inviscid region, and drops to zero in the near-axis boundary layer. Note that there is no viscous layer near the separation cone, $x = x_{S_1}$ in figure 17, where the flow is directed to the apex. It is typical that the viscous jets develop near $x = x_{S_k}$ only when the radial velocity is positive at the separating cone.

4.5.3. *Collapse in the two-cell flow*

Since the flow pattern inside the cone $x_{S_1} < x < 1$ is similar to that in the lower branch of S_1, we have assumed that the collapse can occur in a vicinity of the upper branch of S_2, and our numerical study confirms this conjecture. Curve C_2 in figure 13

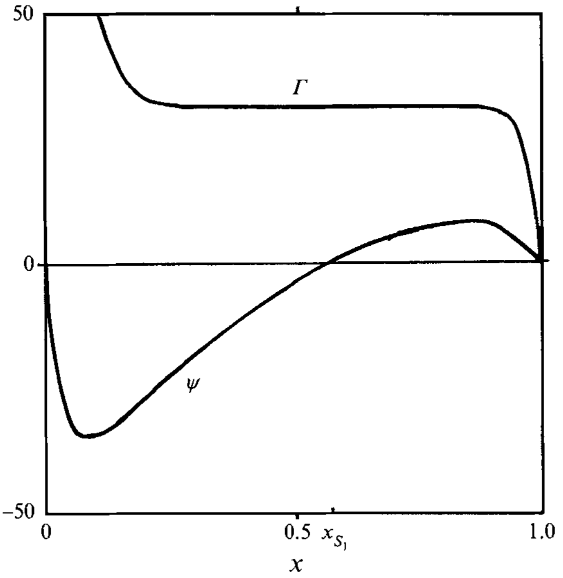

FIGURE 17. Profiles of stream function ψ and circulation Γ for the upper branch of S_2 in figure 13 at $\Gamma_c = 500$. In the near-surface layer, circulation drops from Γ_c at $x = 0$ to the line $\Gamma = 31$.

shows the calculated collapse boundary; there is no regular solution inside the dashed region. We also expect that the collapse occurs between the lower branches of S_2 and S_3, the upper branches of S_3 and S_4, and so on, i.e. in each case when the flow converges to the axis in the near-axis cell. However, based on the results for curve C_2, we think that values of I and Γ_c for the next collapse curves are very large, and therefore we need to develop an advanced numerical technique to check the latter conjecture. Also since the collapse and separation curves merge at large I (see figure 13), we need to calculate one more term in the asymptotic expansion to distinguish between the collapse and separation asymptotes. As the basic subject of this paper is the swirl bifurcation, and the collapse is just a related auxiliary topic, we postpone the problem of the collapse cascade for further study.

4.6. *Self-swirling*

4.6.1. *Linear problem*

We have shown in §2.2 that collapse in now-swirling flows is a sufficient condition for the swirl dynamo in liquid cones of $\theta_c < 90°$. The collapse in the BBF that has been found numerically may also be predicted analytically. First, we show that F_J, given by (34), is positive in the interval $x_c \leqslant x < 1$. Differentiating (34) once gives

$$F_J' = \frac{1-x}{(1-x_c)^2}[f_1(x) - f_1(x_c)], \quad f_1(x) = \frac{1+x}{1-x}\ln\frac{1+x}{2}.$$

Since $f_1(x)$ is a decaying function for $x > -1$, it follows that $f_1(x) < f_1(x_c)$ and, therefore, $F_J' < 0$ inside the interval $x_c < x < 1$. Then, from $F_J(1) = 0$, it follows that $F_J(x) > 0$ for $x < 1$ and, moreover, it decays monotonically as x varies from x_c to 1.

Equation (18), together with conditions (19), can be transformed into the integral form

$$U = 1 - \int_{x_c}^{x} (x-t)\frac{F(t)\,U(t)}{2(1-t^2)^2}\mathrm{d}t. \tag{61}$$

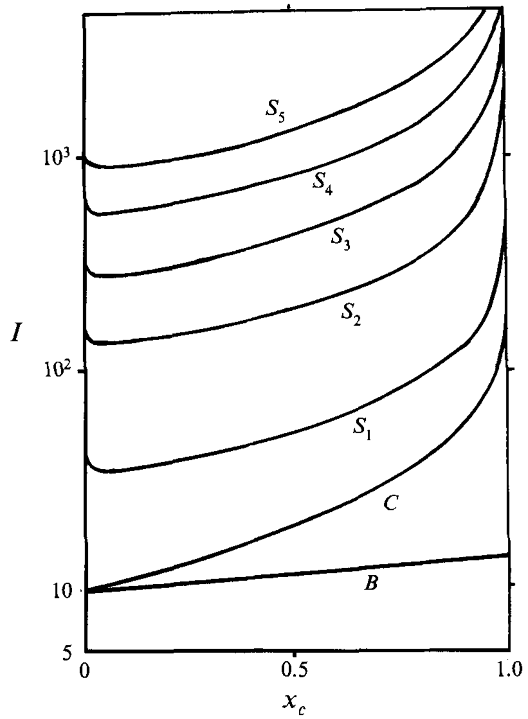

FIGURE 18. Dependence on the cone angle of the values of current I corresponding to the swirl bifurcation (B), collapse of the non-swirling solution (C), and subsequent flow separations (S_1–S_5) for the BFF in a meniscus with a shear-free surface.

Let x_p be the first root of $U(x)$ as x increases from x_c. Suppose that $x_p > 1$ for all I. From (18) it follows that $U'' < 0$ for $U > 0$, and therefore $U > (1-x)/(1-x_c)$ inside the interval $x_c < x < 1$. Then using $(1-x)/(1-x_c)$ instead of U in the right-hand side of (61) and $F = I^2 F_J$, we have

$$U < 1 - \frac{I^2}{1-x_c}\int_{x_c}^{x} (x-t)\,F_J(t)\frac{(1-t)\,\mathrm{d}t}{2(1-t^2)^2}. \tag{62}$$

The integral on the right-hand side of (62) is a positive function independent of I. Then for large enough I, U is negative for any x in the interval $x_c < x < 1$. Thus, the conjecture that $x_p > 1$ is contradicted. Therefore, the collapse must occur at some finite $I = I^*$.

Curve C in figure 18 shows I^* as a function of the cone angle. It has been calculated numerically with the help of the algorithm described in §4.2. Curve B shows $I_*(x_c)$ where swirling solutions appear. To find bifurcation values $I = I_*$, the linear problem for the circulation has been solved numerically with the help of the algorithm similar to that described in §3.3 but with $F = I^2 F_J$.

4.6.2. *Nature of bifurcation*

To solve the nonlinear problem for the self-swirling regimes we integrate the system (3), (13), (42) as an initial-value problem from $x = x_c$ to $x = 1$ with conditions (7), (11), and (62) and some tentative values of $F(x_c)$, Γ_c, and I. Usually $F(x_c)$ and I have been chosen to satisfy (4) and (6), and Γ_c has been used as a free parameter. Figure 19 shows the results for $\theta_c = 45°$. Line 1 at the abscissa corresponds to the non-swirling regime that terminates at $I = I^* = 27.7$ due to the collapse. However, at $I = I_* = 12.7$ the

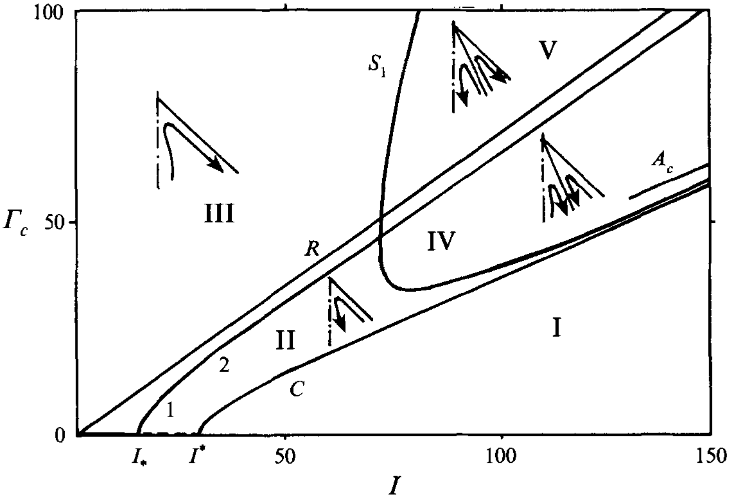

FIGURE 19. Dependence of circulation at the surface Γ_c on current I for the primary (curve 1) and secondary (curve 2) solutions at section $x_c = 0.707$ of figure 18. I_* and I^* correspond to the swirl bifurcation and collapse, respectively. Other notations are the same as in figure 12.

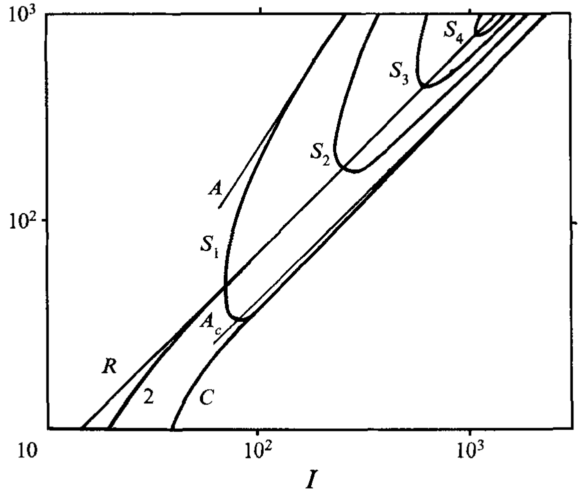

FIGURE 20. As figure 19 but for larger I and Γ_c. Line A is an asymptote for S_1, line A_c is an asymptote for C, and curves S_1–S_4 correspond to subsequent flow separations.

secondary swirling regime appears (curve 2 in figure 19). Since the abscissa, $\Gamma_c = 0$, is a symmetry line, one can see that the supercritical pitchfork bifurcation takes place. Our calculations show that the swirl bifurcation is also supercritical in the whole range of the cone angle, $0 < x_c < 1$. We expect that the primary swirl-free solution becomes unstable after the bifurcation and show it by the dashed line in the interval $I_* < I < I^*$. Curves C, R, and S_1 in figure 19 are similar to those in figure 12, but calculated for $\theta_c = 45°$ here. Each point above the collapse curve C in figure 19 corresponds to a solution at given I and Γ_c, but the self-swirling condition (11) is satisfied only at curve 2.

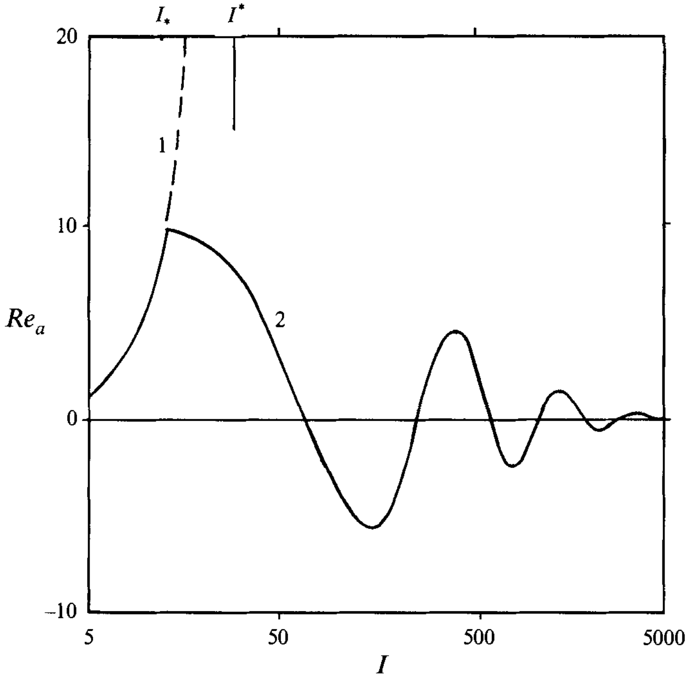

FIGURE 21. Dependence of dimensionless axial velocity Re_a for the primary (curve 1) and secondary (curve 2) regimes. Line $I = I^*$ is an asymptote for curve 1. Zeros of $Re_a(I)$ correspond to the subsequent flow separations.

4.6.3. *Separations in self-swirling flows*

When curve 2 intersects curve S_1 as I increases, the first separation occurs in the self-swirling regime and the flow becomes two-cellular with inflows near both the surface and axis, and an outflow near some intermediate cone $x = x_s$ (see the sketch in region IV of figure 19). The following intersections of curve 2 with curves S_2, S_3, and S_4 shown in figure 20 correspond to the next separations, at which the flow becomes three-, four- and five-cellular, respectively. Since curve 2 is positioned below line R in figures 19 and 20, the flow converges to the cone apex near the liquid surface for all I, but near the axis the flow alternately diverges to or converges from the apex as I increases. Figure 21 shows the dependence of the axial velocity on I calculated for $\theta_c = 45°$. Curve 1 corresponds to the swirl-free regime. Along this curve, Re_a tends to infinity as I approaches the collapse value I^*; however, Re_a decreases just after the bifurcation at $I = I_*$ along curve 2 corresponding to the secondary self-swirling regime. Then as I increases, Re_a oscillates but has a decaying amplitude. Thus, the self-swirling flow becomes multi-cellular. What is a physical reason for this phenomenon?

4.6.4. *Physical mechanism for the separation cascade*

Since the electromagnetic forces are directed toward the axis (see the sketch in figure 11) they induce a converging-to-axis flow when I is small, and the convergence becomes stronger as I increases. When swirl appears at $I > I_*$, it generates centrifugal forces that are directed away from the axis, i.e. opposite to the electromagnetic ones. The converging flow transports circulation to the axis (with a tendency to make the circulation distribution uniform) but the flow does not change the distribution of the electromagnetic forces. As a result, the centrifugal forces become dominant near the axis and this leads to the first separation. When the flow becomes divergent in the near-axis cell, however, it transports the circulation away from the axis. Since circulation is zero at the axis, this convection causes the circulation to decrease in the vicinity of the axis. As a result, the electromagnetic forces overcome the centrifugal ones there and this leads to the second separation, and the corresponding appearance of the third recirculation cell near the axis with a converging-to-axis flow. Now, one can consider this inner cell, and as I increases further, the separation process iterates. This physical image corresponds to the mathematical fact that, as I increases, the first term on the right-hand side of (42) becomes alternately larger or less than the second term in a vicinity of $x = 1$. For an arbitrary given value of circulation at the surface, a balance of electromagnetic and centrifugal forces is possible that corresponds to the meridional motion being at rest (lines R in figures 19 and 20). However, for such an outcome, the special relation (41) between the current and circulation must be satisfied, and this is not the case for the self-swirling motion (compare curves R and 2 in figure 19). So for the self-swirling regime, one has the separation cascade instead of zero meridional motion. At first sight it seems rather striking that the separations occur even when the meridional flow near the axis becomes very slow, as illustrated by the dependence of $Re_a(I)$ shown by curve 2 in figure 21 and which follows from the analysis in §3.4.4 in the vicinity of line R. To study this effect in detail and to find the asymptotic features of the self-swirling flow, we now consider the limiting transition $I \to \infty$.

4.6.5. *Near-surface boundary layer*

One can see in figure 20 that curve 2, corresponding to the self-swirling flow, asymptotically (as I increases) approaches ray R, corresponding to the absence of the meridional motion. This means that the meridional motion becomes weak in comparison with the rotation and the circulation distribution tends to that described by (39) and (41). Nevertheless, the meridional motion stays significantly strong near the surface not to be governed by the linear system (44). To find the asymptotic character of the near-surface flow, one needs a boundary-layer approximation.

Looking for inner variables, we use the transformation

$$\eta = \alpha(x - x_c), \quad \psi = \alpha(1 - x_c^2)\, W(\eta), \quad F = \alpha^2(1 - x_c^2)^2\, \Phi(\eta),$$
$$\Gamma = I[(1 - x) + G(\eta)/\alpha]/[(1 - x_c)\sqrt{2}],$$

in (3), (13), and (22), and in the limit $I \to \infty$, obtain

$$\alpha = I^{2/5}(1 - x_c)^{-4/5}(1 + x_c)^{-3/5}, \quad W' = \Phi + W^2/2, \quad G'' = W(G' - 1), \quad \Phi'' = G, \tag{63}$$

where the prime denotes differentiation with respect to η. Boundary conditions (7), (11), and (32) are transformed to

$$W(0) = 0, \quad G'(0) = (1 - x_c)/(1 + x_c), \quad \Phi'(0) = 0, \tag{64}$$

while (4) and (6) become

$$W, G \to 0 \quad \text{as} \quad \eta \to \infty. \tag{65}$$

The boundary value problem (63)–(65) can be reduced to an initial-value problem by using tentative values for $G(0)$ and $\Phi(0)$. Then we integrate (63) and (64) from $\eta = 0$ to infinity and choose $G(0)$ and $\Phi(0)$ to satisfy (65) with the help of the shooting procedure. Owing to (65), we can linearize (63) to reveal the solution behaviour at large η. This gives

$$W^{\mathrm{v}} + W = 0,$$

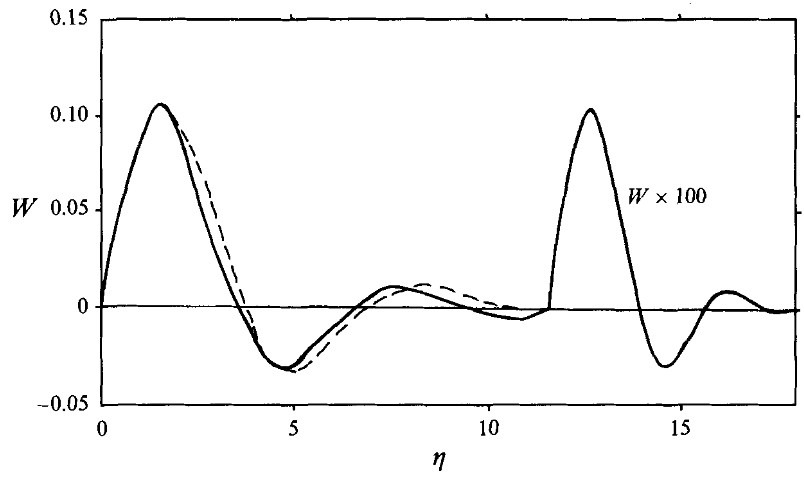

FIGURE 22. Comparison of the stream-function profiles calculated using the full NSE at $I = 5603$ (solid curve) and in the boundary-layer approximation (dashed curve). $x_c = 0.707$.

with the general solution,

$$W = C_1 \exp(-\eta) + \exp(-p_1 \eta)[C_2 \cos(\omega_1 \eta) + C_3 \sin(\omega_1 \eta)] \\ + \exp(p_2 \eta)[C_4 \cos(\omega_2 \eta) + C_5 \sin(\omega_2 \eta)],$$

$$p_1 = \cos(2\pi/5), \quad \omega_1 = \sin(2\pi/5), \quad p_2 = \cos(\pi/5), \quad \omega_2 = \sin(\pi/5).$$

To satisfy (65), C_4 and C_5 must be zero. The first term becomes negligible for $\eta \gg 1$, and, finally, we have $W = C \exp(-p_1 \eta) \sin(\omega_1 \eta + \eta_0)$. Therefore, the number of cells is obtained as $N = \alpha\omega_1(1-x_c)/\pi \sim I^{2/5}$ (note that this result is similar to (60)). The maximum velocity value of the meridional motion is reached at the surface and is characterized by

$$Re = \psi'(x_c) = \Phi(0) I^{4/5}(1-x_c)^{-3/5}(1+x_c)^{-1/5}.$$

Since the maximum azimuthal velocity is characterized by $\Gamma_c = I/\sqrt{2}$, the radial/azimuthal velocity ratio asymptotically tends to zero even in the near-surface layer.

Owing to the second condition (64), the boundary-layer solution depends on x_c. We have calculated $G(0)$ and $\Phi(0)$ in the interval $0 < x_c < 1$ and, in particular, we have found that $G(0) = -0.1772$ and $\Phi(0) = 0.1104$ at $x_c = 0.707$. For this x_c, figure 22 shows $W(\eta)$ calculated in the boundary-layer approximation (dashed curve) and at $I = 5603$ by the algorithm described in §4.6.2. One can see that the curves are close for small η, and this agreement is an additional check on both numerical procedures. The value of I stated above corresponds to the eight flow separation with $\Gamma_c = 3921$ and $Re = 212$. The circulation distribution is very close to (39), with an oscillating deviation whose maximum value is at the surface and less than 1 %.

5. Discussion

5.1. *Comparison of the self-swirling regimes in SSF and BFF*

We have found that for both surface and body forcing the primarily pure meridional flow in the liquid cones with $\theta_c < 90°$ becomes self-swirling owing to the supercritical pitchfork bifurcation. Also, in both SSF and BFF, flow separation occurs as the swirl increases. However, as the swirl grows further, features of the self-swirling flows are different for the surface and body forcing.

For SSF, we have found that (i) the meridional motion is two-cellular, (ii) the inner cell occupies almost the whole flow region except a thin near-surface layer where the outer cell is positioned, (iii) the flow is directed toward the cone apex outside the near-surface layer, (iv) the rotation is weak in comparison with the meridional motion (compare (38) with (40)–(42)), and (v) the rotation is concentrated in the near-surface layer.

These asymptotic features of the self-swirling regime are quite different for body forcing. Indeed, our asymptotic analysis for body forcing has revealed that (i) there is an infinite cascade of flow separation as the electric current I increases, (ii) the thickness of all cells tends to zero as $I^{-2/5}$, (iii) the flow direction alternates in the near-axis cell, (iv) the rotation dominates over the meridional motion, and (v) the circulation distribution is close to that for rigid-body rotation. (Note, to support the latter claim, that (39) can be rewritten as $\Gamma = \Gamma_c[\sin(\theta/2)/\sin(\theta_c/2)]^2 \approx \Gamma_c(\theta/\theta_c)^2$.)

5.2. *Separation cascade in a slow flow*

The infinite cascade of flow separations that we have found for the BFF case should not be too unexpected, despite the meridional flow being very slow, since the flow separation is a nonlinear phenomenon. An infinite sequence of eddies has been shown to exist in a slow flow inside a sharp corner between two rigid planes (Moffatt 1964). In the Moffatt example, the number of circulatory cells is infinite even when the Reynolds number tends to zero, and the size of the cells depends on the corner angle only. However, in our case, the number of cells grows and the size of each cell decays as the intensity of the forcing increases. Our case is closer to the flow in a deep container induced by a tangent force at the fluid surface, where the cell number also increases with the Reynolds number based on the surface velocity.

5.3. *Analogy with the hydromagnetic dynamo*

In the axisymmetric case, the equations for the magnetic induction are similar to that for the circulation and one can expect an analogous effect of magnetic field generation in primarily non-magnetic flows. There are so-called 'anti-dynamo' Cowling's and Braginsky's theorems, see a review and details in Goldshtik & Shtern (1989, 1993), stating that the axisymmetric dynamo is impossible. However, the theorem conditions are not fulfilled for the similarity class considered, and bifurcation of the axisymmetric magnetic induction does occur in a number of conical flows (Goldshtik & Shtern 1989, 1991, 1993; Petrunin & Shtern, 1993). The analogy between the swirl and hydromagnetic dynamo is also manifested in the asymptotic behaviour. Both the swirl and electric current are concentrated in a near-surface boundary layer as *Re* increases for SSF.

The magnetic induction and velocity decay weakly, $\sim r^{-1}$ as $r \to \infty$, in the similarity class, whereas Braginsky's condition requires the decay to be as r^{-3}, at least. In particular, this means that the generation of the swirl and magnetic induction in conical flows is a large-scale process and is not localized in a small vicinity of the origin. Our recent studies support this claim, showing the instability nature of the appearance of swirl (Shtern & Barrero 1995) and induction (Shtern 1995).

5.4. *Instability mechanism*

The weak decay of the self-swirling solution at infinity (the circulation does not decay at all) poses the question whether the bifurcation in the similarity class is related to the instability and bifurcation of a realistic non-similar flow. The similarity solutions can approximate realistic flows only in some region, $r_i < r < r_o$, say, outside the vicinities

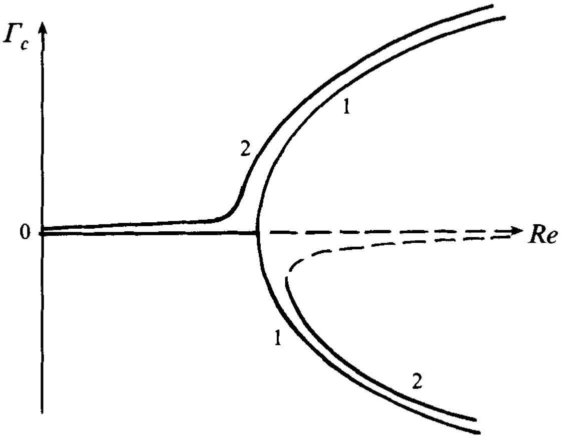

FIGURE 23. Destruction (curve 2) of the pitchfork bifurcation (curve 1) for a non-similar flow.

of the meniscus apex and the capillary rim in electrosprays. Some deviations from the similarity are unavoidable at $r = r_i$ and $r = r_o$. How do these disturbances influence the flow inside the region? It has been found that such disturbances decay for $Re < Re_*$. However, for $Re > Re_*$, a disturbance at the *outer* boundary, $r = r_o$, grows (as r decreases) triggering the transition to the secondary swirling regime. This disturbance corresponds to a weak swirl at $r = r_o$ which is induced, say, by some asymmetry of the capillary tube. For $Re \ll Re_*$ the induced rotation is of solid-body type and the circulation rapidly decays to the apex. For $Re > Re_*$, a kind of pumping mechanism acts. Owing to the circulatory character of the flow, the angular momentum (which is proportional to the circulation) is transported from the rim to the apex near the meniscus surface. When the liquid flows from the apex to the rim near the axis, a part of the angular momentum is not transported back but is transferred from the axis to the surface by viscous diffusion. This positive feedback results in cumulation of the circulation in the similarity region. As a result, the circulation value in the similarity region can become sufficiently larger than that near the rim. The cumulation process is saturated by the nonlinear effect: the cumulated swirl makes the meridional motion weaker (see curve 2_l in figure 8). This decreases the transport and, therefore, the normal-to-axis transfer of swirl. Finally, the viscous diffusion in the r- and θ-directions reaches a balance at the secondary similarity regime. According to this physical interpretation, the circulatory character of the flow (i.e. inflow near the surface and outflow near the axis) is crucial for the cumulation to occur. A geometrical form of the meniscus (whether it is exactly conical or not) seems to be not so crucial for the pumping mechanism (but the use of the conical approximation drastically eases the analysis!).

5.5. *Destroyed bifurcation*

The above instability features and physical mechanism correspond to the slightly 'destroyed' bifurcation shown in figure 23. Let Γ_c be the circulation on the meniscus surface at some distance r from the apex. Also, let this value of r belong to the similarity region, $r_i < r < r_o$. Curve 1 shows an 'ideal' supercritical pitchfork bifurcation following from our results for the similarity problem. Curve 2 shows a destroyed bifurcation which seems to be relevant for a realistic flow. Along the upper branch of curve 2, Γ_c is not zero at any Re. However, for $Re < Re_*$, Γ_c is proportional to its value at the rim (Γ_o) and can be very small and hardly observable. In contrast, for $Re > Re_*$, Γ_c does not depend on Γ_o, is close to its similarity value in the secondary regime, and can be rather large. Such a scenario agrees with our experimental observations. At small values of a control parameter, swirl is not observed, but when the parameter is increased, swirl becomes so strong that the flow in the 1 mm meniscus looks like a tornado! Moreover, vortex breakdown occurs and the corresponding separation 'bubble' takes a conical form that agrees with the separation prediction in this paper. These observations of vortex breakdown in the meniscus are preliminary and need further study.

This work was performed under the auspices of the Dirección General de Investigación Científica y Técnica (DGICYT) of Spain (PB90 – 1023). V.S. acknowledges the financial support from the sabbatical program of DGICYT. The authors thank JFM referees for their valuable comments.

REFERENCES

BAILEY, A. G. 1988 *Electrostatic Spraying in Liquids*. John Wiley.

BARRERO, A., FERNANDEZ-FERIA, R., GAÑAN-CALVO, A. M. & FERNANDEZ DE LA MORA, J. 1995*a* The role of liquid viscosity and electrical conductivity on the motions inside Taylor cones. *Manuscript in preparation.*

BARRERO, A., GAÑAN-CALVO, A. M. & DAVILA, J. 1995*b* Measurements of droplet size and charge in the electrospraying of liquids. I. Scaling laws for polar liquids. *Aerosol Sci. Technol.* (submitted).

BOJAREVICS, V., FREIBERGS, J. A., SHILOVA, E. I. & SHCHERBININ, E. V. 1989 *Electrically Induced Vortical Flows.* Kluwer.

BOJAREVICS, V., SHARAMKIN, V. L. & SHCHERBININ, E. V. 1977 Effect of longitudinal magnetic field on the medium motion in electrical arc welding. *Magnetohydrodynamics* **13**, 115–120.

BURRGRAF, O. R. & FOSTER, M. R. 1977 Continuation or breakdown in tornado-like vortices. *J. Fluid Mech.* **80**, 685–704.

FENN, J. B., MANN, M., MENG, C. K., WONG, C. F. & WHITEHOUSE, C. 1989 Electrospray ionization for mass spectrometry of large biomolecules. *Science* **246**, 64–71.

FERNANDEZ DE LA MORA, J. 1992 The effect of charge emission from electrified liquid cones. *J. Fluid Mech.* **243**, 561–574.

FERNANDEZ DE LA MORA, J., FERNANDEZ-FERIA, R. & BARRERO, A. 1991 Theory of incompressible conical vortices at high Reynolds numbers, *Bull. Am. Phys. Soc.* **36**, 2619.

FERNANDEZ DE LA MORA, J. & LOSCERTALES, I. G. 1994 The current emitted by highly conducting Taylor cones. *J. Fluid Mech.* **260**, 155–184.

FERNANDEZ-FERIA, R., FERNANDEZ DE LA MORA, J. & BARRERO, A. 1995 Conically similar swirling flows at high Reynolds numbers flows. Part 1. One-cell solutions, high Reynolds number. *SIAM J. Appl. Maths* (submitted).

FUNAKOSHI, M. & INOUE, S. 1988 Surface waves due to resonant horizontal oscillation. *J. Fluid Mech.* **192**, 219–247.

GAÑAN-CALVO, A. M. 1995 The electrohydrodynamics of the cone-jet electrospraying. *J. Fluid Mech.* (submitted).

GOLDSHTIK, M. A. 1960 A paradoxical solution of the Navier–Stokes equations. *Appl. Mat. Mech. (Sov.)* **24**, 610–621.

GOLDSHTIK, M. A. & SHTERN, V. N. 1988 Conical flows of fluid with variable viscosity. *Proc. R. Soc. Lond.* A **419**, 91–106.

GOLDSHTIK, M. A. & SHTERN, V. N. 1989 Self-similar hydromagnetic dynamo. *Sov. Phys., J. Exp. Theor. Phys.* **96**, 1728–1743.

GOLDSHTIK, M. A. & SHTERN, V. N. 1990 Collapse in conical viscous flows. *J. Fluid Mech.* **218**, 483–508.

GOLDSHTIK, M. A. & SHTERN, V. N. 1991 Bifurcation in near-star convection. *Eur. J. Mech.* B/*Fluids* **10** (n 2, Suppl.), 49–54.

GOLDSHTIK, M. A. & SHTERN, V. N. 1993 Axisymmetric hydromagnetic dynamo. *Prog. Astronaut. Aeronaut.* **149**, 87–102.

GOLDSHTIK, M. A., SHTERN, V. N. & ZHDANOVA, E. M. 1984 Onset of self-rotation in a submerged jet. *Sov. Phys. Dokl.* **277**, 815–818.

HAYATI, I., BAILEY, A. I. & TADROS, TH. F. 1986*a* Mechanism of stable jet formation in electrohydrodynamic atomisation. *Nature* **319**, 41–43.

HAYATI, I., BAILEY, A. & TADROS, TH. F. 1986*b* Investigations into the mechanism of electrohydrodynamic spraying of liquids. II Mechanism of stable jet formation and electrical forces acting on a liquid cone. *J. Colloid Interface Sci.* **117**, 222–230.

KAWAKUBO, M., TSUCHIA, Y., SUGAYA, M. & MATSUMURA, K. 1978 Formation of a vortex around a sink: A kind of phase transition in a nonequilibrium open system. *Phys. Lett.* A **68**, 65–66.

LONG, R. R. 1961 A vortex in an infinite viscous fluid. *J. Fluid Mech.* **11**, 611–624.

LUNDQUIST, S. 1969 On the hydromagnetic viscous flow generated by a diverging electric current. *Ark. Fys.* **40**, 85–95.

MOFFATT, H. K. 1964 Viscous and resistive eddies near a sharp corner. *J. Fluid Mech.* **18**, 1–18.

NARAIN, J. P. & UBEROI, M. S. 1971 Magnetohydrodynamics of conical flows. *Phys. Fluids* **25**, 2687–2692.

OGAWA, A. 1993 *Vortex flows*, pp. 215–221. CRC Press.

PANTANO, C., GAÑAN, A. M. & BARRERO, A. 1994 Zerouth order, electrostatic solution for electrospraying in cone-jet mode. *J. Aerosol Sci.* (to appear).

PAULL, R. & PILLOW, A. F. 1985 Conically similar viscous flows. Part 3. Characterisation of axial causes in swirling flows and one-parameter flow generated by a uniform half-line source of kinematic swirl angular momentum. *J. Fluid Mech.* **155**, 359–380.

PETRUNIN, A. A. & SHTERN, V. N. 1993 Bifurcations in MHD flow generated by electric current discharge. *Prog. Astronaut. Aeronaut.* **149**, 116–130.

SHCHERBININ, E. V. 1969 On a kind of exact solution in the magnetohydrodynamics. *Magnetohydrodynamics* **5** (4), 46–58.

SHERCLIFF, J. A. 1970 Fluid motion due to an electric current source. *J. Fluid Mech.* **40**, 241–250.

SHTERN, V. 1995 Cosmic jets as a pump for magnetic field. *Phys. Lett.* A (accepted).

SHTERN, V. & BARRERO, A. 1994 Striking features of fluid flows in Taylor cones related to electrosprays. *J. Aerosol Sci.* **25**, 1049–1063.

SHTERN, V. & BARRERO, A. 1995 Instability nature of swirl appearance in liquid cones. *Phys. Rev.* E **52**, 627–635.

SHTERN, V., GOLDSHTIK, M. & HUSSAIN, F. 1994 Generation of swirl due to symmetry breaking. *Phys. Rev.* E **49**, 2881–2886.

SHTERN, V. & HUSSAIN, F. 1993 Hysteresis in a swirling jet as a tornado model. *Phys. Fluids* A **5**, 2183–2195.

SHTERN, V. & HUSSAIN, F. 1995 Hysteresis in swirling jets. *J. Fluid Mech.* (submitted).

SOZOU, C. 1971 On fluid motion induced by electric current source. *J. Fluid Mech.* **49**, 25–32.

SOZOU, C. 1992 On solutions relating to conical vortices over a plane wall. *J. Fluid Mech.* **244**, 633–644.

SOZOU, C. & PICKERING, W. M. 1976 Magnetohydrodynamic flow due to the discharge of an electric current in a hemispherical container. *J. Fluid Mech.* **73**, 641–650.

SQUIRE, B. 1952 Some viscous fluid flow problems. 1. Jet emerging from a hole in a plane wall. *Phil. Mag.* **43**, 942–945.

TAYLOR, G. I. 1964 Disintegration of water drops in an electric field. *Proc. R. Soc. Lond.* A **280**, 383–397.

TORRANCE, K. E. 1979 Natural convection in thermally stratified enclosures with localised heating from below. *J. Fluid Mech.* **95**, 477–495.

YATSEEV, V. N. 1950 On a class of exact solutions of the viscous fluid motion equations. *Sov. Phys., J. Exp. Theor. Phys.* **20**, 2147–2157.

ZELENY, J. 1917 Instability of electrified liquid surface. *Phys. Rev.* **10**, 1–6.

ZHIGULEV, V. N. 1960 On ejection effect due to an electric current discharge. *Sov. Phys. Dokl.* **130**, 280–283.